Arbitrary entangled state transfer via a topological qubit chain

Chong Wang, Linhu Li, Jiangbin Gong, and Yu-xi Liu

Phys. Rev. A **106**, 052411 — Published 10 November 2022

DOI: 10.1103/PhysRevA.106.052411

Arbitrary entangled state transfer via a topological qubit chain

Chong Wang,[1,2] Linhu Li,[3] Jiangbin Gong,[4,5,*] and Yu-xi Liu[1,2,†]

[1] *School of integrated circuits, Tsinghua University, Beijing, 100084, China*
[2] *Frontier Science Center for Quantum Information, Beijing, China*
[3] *Guangdong Provincial Key Laboratory of Quantum Metrology and Sensing & School of Physics and Astronomy, Sun Yat-Sen University (Zhuhai Campus), Zhuhai 519082, China*
[4] *Department of Physics, National University of Singapore, Singapore 117542, Singapore*
[5] *Centre for Quantum Technologies, National University of Singapore, 117543, Singapore*

(Dated: September 23, 2022)

Quantum state transfer is one of the basic tasks in quantum information processing. We here propose a theoretical approach to realize arbitrary entangled state transfer through a qubit chain, which is a class of extended Su-Schrieffer-Heeger models and accommodates multiple topological edge states separated from the bulk states. We show that an arbitrary entangled state, from 2-qubit to $\mathcal{N}$-qubit, can be encoded in the corresponding edge states, and then adiabatically transferred from one end to the other of the chain. The dynamical phase differences resulted from the time evolutions of different edge states can be eliminated by properly choosing evolution time. Our approach is robust against both the qubit-qubit coupling disorder and the evolution time disorder. For the concreteness of discussions, we assume that such a chain is constructed by an experimentally feasible superconducting qubit system, meanwhile our proposal can also be applied to other systems.

I. INTRODUCTION

There are many possible platforms to realize quantum computation [1–3], e.g., cold atoms [4–7], trapped ions [7–15], and superconducting quantum circuits [16–28]. On these platforms, quantum state transfer (QST) in a controllable way [3, 29] is one of crucial requirements. Though long-distance quantum communication has been widely achieved in optical fibers and free-space [30–34], it is still very important to find a promising way for transferring quantum states through solid-state devices or condensed matter [35–42]. A number of QST protocols have been proposed for different solid-state medium [43–52]. In recent years, QST via a spin chain has attracted extensive attentions [35–37] and many technologies have already been developed [50–58].

Perfect QST can be realized through well designed spin chain with invariable couplings [59–63]. Meanwhile, it can also be realized by precisely modulating the spin-spin couplings [64–67]. For example, quantum states can be transferred by simply applying a sequence of SWAP operations implemented by π pulses between the pairs of nearest neighboring sites [60], which needs only the spin-spin couplings to be switched on and off periodically [68]. Nevertheless, these known methods require the accurate design of the system Hamiltonian, thus are usually less robust against disorders and imperfections in large-scale implementations. To overcome this issue, adiabatic QST protocols have been widely studied [37, 69–77], as the QST exploiting the adiabatic theorem [78, 79] is independent of the protocol operation details so long as the evolution of the system is slow enough.

Our QST method here is based on the spectral and dynamical features of a topological qubit chain. For topological insulators, robust conducting edge states are guaranteed by the nontrivial topology of bulk bands [80–83]. These edge states are insensitive to smooth changes in the system parameters unless a topological phase transition occurs [80, 81]. Such robustness based on topological protection provides topological quantum systems a great potential for quantum information and quantum computing [84–89]. The Su-Schrieffer-Heeger (SSH) chain [90] is the simplest model of the topological insulators and can be realized by a qubit chain with staggered couplings when the qubit chain is restricted to the subspace of single excitation [91].

Building on the concepts of topological edge states and adiabatic QST via a qubit chain, protocols for efficient QST [55–58, 92, 93] have also been proposed, with more robustness to disorder due to the underlying topological protection. With specific design of topological qubit chains, quantum states can be encoded in edge states of the systems, and transferred from one end of the chain to the other by adiabatically altering couplings between qubits [55–57, 93]. However, most of these available proposals focus on single qubit state transfer, and multi-qubit state transfer with arbitrary entanglement is still a challenging task. Recently, a more advanced protocol for QST via the so-called Floquet topological edge modes was proposed [69]. In this protocol, some entangled states are encoded in the edge states of quasienergy zero and π modes, and the high-fidelity transfer of entangled states can be achieved over a long distance. However, this method requires additional dynamical modulation on the time-periodic couplings between the qubits and may pose new experimental challenges.

In our method, arbitrary entangled state can be encoded in topological edge states, which are supported by a generalized SSH chain. As the parameters of the

* phygj@nus.edu.sg
† yuxiliu@mail.tsinghua.edu.cn

system are slowly altered, the edge states can be adiabatically transferred from one end of the chain to the other. Thus the entangled state can be transferred along this adiabatic passage. It is well known that the adiabatic evolution leads to two phases, i.e, geometric phase and dynamical phase. The geometric phase can be easily wiped out with a chosen gauge in non-closed adiabatic evolution [79], and the dynamical phase can be eliminated when the evolution time is carefully chosen. Thus, the quantum phases between different components encoding an entangled state can be well-controlled or recovered, and the entangled state can be truly transferred.

For the concreteness of discussions, we assume that the qubit chain is formed by the superconducting quantum circuits, which have been developing rapidly [16–18]. In particular, superconducting qubit chains have been widely studied for simulating many-body quantum physics [94–96]. There are several advantages to use superconducting qubits as quantum simulators. First, superconducting qubits are highly coherent with long coherence time ($10 \sim 100\mu s$) [97, 98]. Second, most of the parameters of superconducting qubits are highly controllable [99–103], thus we can perform rather arbitrary operation on the systems. Third, the superconducting quantum circuits have high scalability and designability. One quantum chip can support a large number of controllable qubits with different connecting manners [104]. These advantages make superconducting quantum circuits one of the best platforms to perform quantum simulation and quantum computing. Moreover, the topological chain constructed by superconducting qubits has already been experimentally demonstrated [105]. Thus, for the state-of-the-art, superconducting qubit circuits are very suitable to construct such a chain for QST. The system parameters considered in this work are all based on the existing experiments of Xmon qubits [99–101].

The paper is organized as follows. In Section II, we introduce a generalized SSH model, in which each unit cell contains three qubits, and the topology of the model is characterized by winding number. We also use Xmon qubits as an example to show how to form such generalized model. In Section III, we derive the edge states of the Hamiltonian given in Section II for the generalized SSH model, and then show that arbitrary two-qubit entangled state can be encoded in these edge states and transferred from one end of the chain to the other through adiabatic process. The exact dynamical solution based on adiabatic theorem is also given. Furthermore, we illustrate the robustness of our proposal against disorder from two parts, i.e., the coupling strength and evolution time. In Section IV, we generalize QST from the entangled state of the two-qubit to those of $\mathcal{N}$-qubit with $\mathcal{N} \geq 3$. In particular, the QST of three-qubit state is carefully analyzed. In Section VI, we further discuss our proposal and analyze the experimental feasibility, and finally summarize our results.

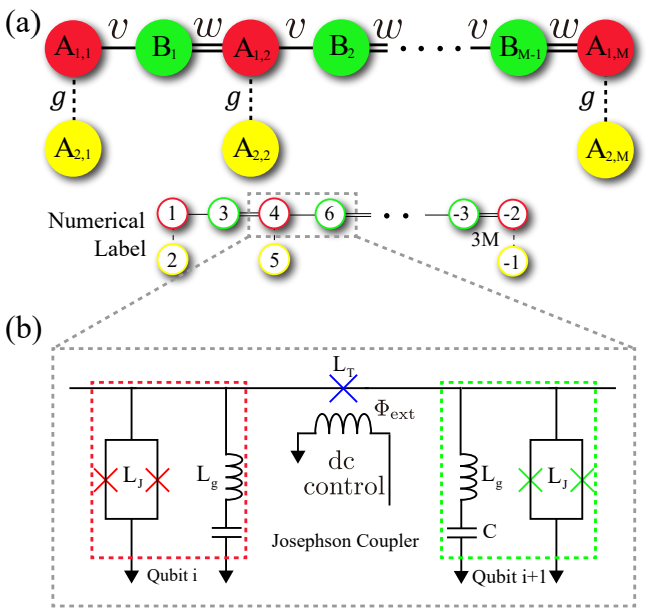

Figure 1. (a) Schematic diagram of a one-dimensional qubit chain. Each unit cell hosts three qubits, labelled as $A_{1,m}$, $A_{2,m}$ and B_m separately (The first subscript of A denotes the intracell index. The subscript of B and the second subscript of A denote the intercell index). The coupling strength g between $A_{1,m}$ and $A_{2,m}$ is uniform along the chain, whereas the hopping between $A_{1,m}$ and B_m is staggered, denoted as v and w. Each qubit can also be labeled by one unique numerical index x in order of $A_{1,1}A_{2,1}B_1A_{1,2}\cdots B_{M-1}A_{1,M}A_{2,M}$. (b) Realization of the qubit chain with Xmon qubits. Each qubit contains three basic superconducting circuits elements, i.e, the josephson junction, the capacitance and the inductance. Two adjacent qubits are coupled through a Josephson coupler. The qubit-qubit coupling can be tuned via an external magnetic flux Φ_{ext} with a dc control. The Josephson junctions labeled L_J are each double junctions threaded by additional fluxes (not shown) that tune the qubit frequencies. Therefore, both the qubit frequencies and the couplings in the qubit chain are tunable.

II. GENERALIZED SSH MODEL WITH THREE QUBITS IN EACH UNIT CELL

The SSH model [90] is one of the simplest examples hosting one-dimensional topological phases. This model and its various extensions have been widely used to study different physical phenomena [106–113]. In the standard SSH model, each unit cell has two sublattices. By contrast, for one class of extended SSH models, each unit cell contains 3 or more sublattices, thus called the SSH3 or SSHN models [114, 115]. As schematically shown in Fig. 1(a), we first consider a extended SSH3 model consisting of a qubit chain with M unit cells. Hereafter, we use the unit cell number M to denote the length of the chain. Each unit cell contains three sublattices labelled as $A_{1,m}$, $A_{2,m}$, and B_m with $m = 1, 2, \cdots, M$. The sublattice B_M of the Mth unit cell is removed from the right

end of the chain. Sublattices $A_{1,m}$ and B_m are analogous to those in the standard two-band SSH model with staggered coupling strengths v and w. An extra sublattice $A_{2,m}$ is coupled to $A_{1,m}$ with the coupling strength g ($g > 0$). Thus, the Hamiltonian of such a qubit chain is ($\hbar = 1$)

$$H = \sum_{m=1}^{M-1} \left(v\sigma_{A_{1,m}}^{+}\sigma_{B_m}^{-} + w\sigma_{A_{1,m+1}}^{+}\sigma_{B_m}^{-} + \text{H.c.} \right) + \sum_{m=1}^{M} \left(g\sigma_{A_{1,m}}^{+}\sigma_{A_{2,m}}^{-} + \text{H.c.} \right). \quad (1)$$

with m denoting the index of each unit cell. The ladder operators in the mth unit cell is given by $\sigma_I^+ = |e_I\rangle\langle g_I|$ ($I = A_{1,m}, A_{2,m}, B_m$), with $|e_I\rangle$ and $|g_I\rangle$ denoting the excited and ground states, and the operator σ_I^- is the Hermitian conjugate of the operator σ_I^+.

We note that our proposal can be applied to any kinds of controllable qubit systems. However, for the concreteness of the studies, we use superconducting qubit circuits, e.g., Xmon qubits, to construct our theoretical model. This X-shape qubit has several advantages, e.g., high-coherence, fast tunable coupling, and easy connection [99–101], thus is more suitable for our proposal. Our proposal is not limited to the Xmon qubit, and can also be applied to other types of superconducting qubits, e.g., transmon or flux qubit. For our setup, as shown in Fig. 1(b), two Xmon qubits are connected with each other by a Josephson junction coupler [99, 100]. An extra magnetic flux bias Φ_{ext} is applied to tune the effective linear inductance of the coupler junction. Thus, the coupling constant between these two qubits is tunable with controllable extra magnetic flux Φ_{ext} (see details in Appendix A).

In the following studies, we only consider the single-excitation of the chain, thus the Hamiltonian can be rewritten as

$$H = \sum_{m=1}^{M-1} (v|\mathcal{A}_{1,m}\rangle\langle\mathcal{B}_m| + w|\mathcal{A}_{1,m+1}\rangle\langle\mathcal{B}_m| + \text{H.c.}) + \sum_{m=1}^{M} (g|\mathcal{A}_{1,m}\rangle\langle\mathcal{A}_{2,m}| + \text{H.c.}) \quad (2)$$

in the single-excitation subspace $\{|\mathcal{A}_{1,m}\rangle, |\mathcal{A}_{2,m}\rangle, |\mathcal{B}_m\rangle\}$, with $|\mathcal{A}_{1,m}\rangle = \sigma_{A_{1,m}}^{+}|G\rangle$, $|\mathcal{A}_{2,m}\rangle = \sigma_{A_{2,m}}^{+}|G\rangle$ and $|\mathcal{B}_m\rangle = \sigma_{B_m}^{+}|G\rangle$. Here $|G\rangle$ denotes that all qubits in the chain are in the ground state, i.e., $|G\rangle = |g_{A_{1,1}} g_{A_{2,1}} g_{B_1} \cdots g_{A_{2,M}}\rangle$, which is written as $|G\rangle = |gg\cdots g\rangle$ for simplicity.

For the standard two-band SSH model, the topologically nontrivial phase is characterized by a nonzero winding number. Two topological in-gap edge modes are degenerate at zero energy in the thermodynamic limit [82]. However, for a finite lattice size, the two edge states hybridize due to finite-size effect and so that their energy eigenvalues are shifted by an exponentially small amount. Dynamics-wise, this edge-state hybridization would then induce Rabi oscillation between two topological edge modes if the initial state is prepared by exciting the leftmost or rightmost qubit only [116]. To obtain a steady edge state in a finite-size system, one may remove one edge qubit from the standard SSH chain [55, 105]. In this case, this imperfect SSH chain only supports one edge state. This is useful for our considerations here since we are considering the same platform. Indeed, applying this idea of eliminating one edge qubit from an extended SSH model, we can likewise engineer steady edge states in the extended SSH setting, as shown below.

For our extended SSH3 model shown in Fig. 1(a), the Hilbert space of the Hamiltonian is enlarged by the extra qubits $A_{2,m}$ compared with the standard SSH model. The edge states are expected to form from two renormalized branches of the qubit chain, thus resulting in the upper and the lower edge states with positive and negative eigenenergies, as discussed further in Appendix B. To see the topological aspect of these edge states, we first consider the case with $g = 0$, where sublattices $A_{1,m}$ and B_m are decoupled from $A_{2,m}$. In this case, the imperfect SSH model with an odd number of qubits is formed, where v and w are the intra- and inter- cell couplings. In the standard SSH model, edge states appear when the coupling strength at the edge is weaker than the coupling next to it. Similarly, for the imperfect SSH model, a weaker coupling strength appears at the left (right) edge and generates an edge state there when $v < w$ ($v > w$). Therefore, in the presence of an odd number of sites, the system always has one edge state in the topologically nontrivial regime [55]. That is, in our extended SSH3 model, either the left or the right edge state corresponds to a winding number of 1 for the Fourier transformed Hamiltonian (in momentum space), with unit cells defined either as sites $(A_{1,m}, A_{2,m}, B_m)$ or as sites $(B_m, A_{1,m+1}, A_{2,m+1})$ in Fig. 1(a) respectively. When $g = 0$, the edge state is only located at the sublattice $A_{1,m}$, which returns to the case of the standard SSH chain. When $g > 0$, the edge states are expected to occupy both sublattices $A_{1,m}$ and $A_{2,m}$, because they take the role of the A-type sublattice in the standard SSH chain (see Appendix C). With this understanding, we can see that the edge states in our extended SSH model do originate from the topological edge states in the standard SSH model, and hence should be robust to local disorder.

Below we show how such edge states in the extended SSH chain can be used to robustly transfer arbitrary entangled states. We here emphasize that the parameters used for the following numerical simulations are taken from superconducting qubit circuits, e.g., Xmon qubit circuits [99–101].

III. 2-QUBIT ENTANGLMENT STATE TRANSFER

A. Edge states of the qubit chain

In our extended SSH model, there are $\mathcal{L} = 3M - 1$ qubits in the chain when one B-type qubit at the right end of the chain is removed. Let us first give an ansatz that the resultant edge state in our system exclusively occupies sublattices $A_{1,m}$ and $A_{2,m}$ (see appendix B), i.e., the associated wavefunction can be written as

$$|\Psi_{\text{edge}}\rangle = \sum_{m=1}^{M} \lambda^m \left(a\sigma^+_{A_{1,m}} + b\sigma^+_{A_{2,m}}\right)|G\rangle. \tag{3}$$

As energy-eigenstates of the system's Hamiltonian, the wavefunction in Eq. (3) must satisfy the stationary Schrödinger equation

$$H|\Psi_{\text{edge}}\rangle = E|\Psi_{\text{edge}}\rangle. \tag{4}$$

Combining Eq. (1) with Eq. (3), we have

$$\begin{aligned} E\left(a\sigma^+_{A_{1,m}} + b\sigma^+_{A_{2,m}}\right)|G\rangle = a\left(v + w\lambda\right)\sigma^+_{A_{2,m}}|G\rangle \\ + g\left(b\sigma^+_{A_{1,m}} + a\sigma^+_{A_{2,m}}\right)|G\rangle. \end{aligned} \tag{5}$$

It is straightforward to get $v + w\lambda = 0$, i.e., $\lambda = -v/w$, and the coefficients a and b satisfy the following equation as

$$\begin{pmatrix} 0 & g \\ g & 0 \end{pmatrix}\begin{pmatrix} a \\ b \end{pmatrix} = E\begin{pmatrix} a \\ b \end{pmatrix}. \tag{6}$$

Thus, the energy eigenvalues of the edge states are given by $E_\pm = \pm g$, with coefficients (a, b) being $(1/\sqrt{2}, 1/\sqrt{2})$ or $(1/\sqrt{2}, -1/\sqrt{2})$ respectively. This explicit edge state solution indicates that there are two edge states with the form of the Bell state $|\chi_{m,\pm}\rangle = \left(|\mathcal{A}_{1,m}\rangle \pm |\mathcal{A}_{2,m}\rangle\right)/\sqrt{2}$ in each unit cell. The wavefunctions corresponding to the edge states hence take the following form (unnormalized)

$$|\Psi_\pm\rangle = \sum_{m=1}^{M} \lambda^m \left(\frac{\sigma^+_{A_{1,m}} \pm \sigma^+_{A_{2,m}}}{\sqrt{2}}\right)|G\rangle, \tag{7}$$

where both the upper (labeled as $+$) and lower (labeled as $-$) edge states only occupy the A-type qubits. When $|\lambda| = v/w \ll 1$, i.e., $v \ll w$, the edge states are mostly localized in the left end of the chain as

$$|\Psi_\pm\rangle \approx |L_\pm\rangle = \frac{1}{\sqrt{2}}\left(\sigma^+_{A_{1,1}} \pm \sigma^+_{A_{2,1}}\right)|G\rangle. \tag{8}$$

In the limit of $v = 0$, the qubit chain degenerates into $M - 1$ trimers and an additional dimer, an exact edge state $|L_\pm\rangle$ can be obtained at the left end of the chain. When $|\lambda| = v/w \gg 1$, i.e., $v \gg w$, the edge states are mostly localized in the right end of the chain as

$$|\Psi_\pm\rangle \approx |R_\pm\rangle = \frac{1}{\sqrt{2}}\left(\sigma^+_{A_{1,M}} \pm \sigma^+_{A_{2,M}}\right)|G\rangle. \tag{9}$$

In the limit of $w = 0$, an exact edge state $|R_\pm\rangle$ can be obtained at the right end of the chain.

In Fig. 2(a), as an example, the energy spectrum of a 14-qubit chain with 5 unit cells is plotted for $|\lambda| = v/w \in [0, \infty]$. It clearly shows that the two topological edge modes (color-dashed lines) exist in the gaps of three bulk bands. The bulk band in the middle of two edge modes is 4-fold degenerate as shown in Fig 2(b). As the parameter λ changes from 0 to ∞, the localized topological edge states as a function of λ also change their qualitatively behavior, namely, from being localized at the left end (red) to being localized at the right end (green). Meanwhile, the eigenvalues $E_\pm$ corresponding to these two edge states keep constants all along.

B. QST process for arbitrary two-qubit entangled states

According to the quantum adiabatic theorem, if the parameters of the qubit chain in Eq. (1) can be changed slowly enough, it will remain in its instantaneous eigenstate. At $v = 0$, the leftmost two qubits $A_{1,1}$ and $A_{2,1}$ are isolated and the edge states are $|L_\pm\rangle = |\chi_{1,\pm}\rangle|gg\cdots g\rangle$. At $w = 0$, the rightmost two qubits $A_{1,M}$ and $A_{2,M}$ are isolated and the edge states are $|R_\pm\rangle = |gg\cdots g\rangle|\chi_{M,\pm}\rangle$. It is obvious that the coupling strengths

$$v = J\left[1 - \cos\left(\omega t\right)\right], w = J\left[1 + \cos\left(\omega t\right)\right], \tag{10}$$

can be changed slowly, then the state of the left end can be transferred to the right end of the chain. Where ω and J are the frequency and strength of the control field, respectively. For example, as shown in Fig. 2(a), if the system is initially prepared to the state $|L_\pm\rangle$ for the time $t = 0$, then this state adiabatically evolves from $|L_\pm\rangle$ to $|R_\pm\rangle$ when the time t slowly varies from 0 to π/ω. The adiabatic following is feasible here because the considered state is the system's edge state, which is gapped from the bulk states.

In above, we analyze QST when the edge state is the initial state. Let us now consider the general situation that the system is initially prepared to an arbitrary entangled state

$$|\Psi_{\text{in}}\rangle = \left(\alpha\sigma^+_{A_{1,1}} + \beta\sigma^+_{A_{2,1}}\right)|G\rangle, \tag{11}$$

at the left end of the chain, which can be decomposed as

$$|\Psi_{\text{in}}\rangle = \frac{\alpha + \beta}{\sqrt{2}}|L_+\rangle + \frac{\alpha - \beta}{\sqrt{2}}|L_-\rangle. \tag{12}$$

For such more general situation involving the superpositions of two edge states, one must carefully analyze the quantum phases. In an adiabatic process, if the system is initially prepared to an eigenstate $|\Phi\left(0\right)\rangle$, then the final state at the time t is given as

$$|\psi_{\text{ad}}\left(t\right)\rangle = e^{ir(t)}e^{i\theta(t)}|\Phi\left(t\right)\rangle, \tag{13}$$

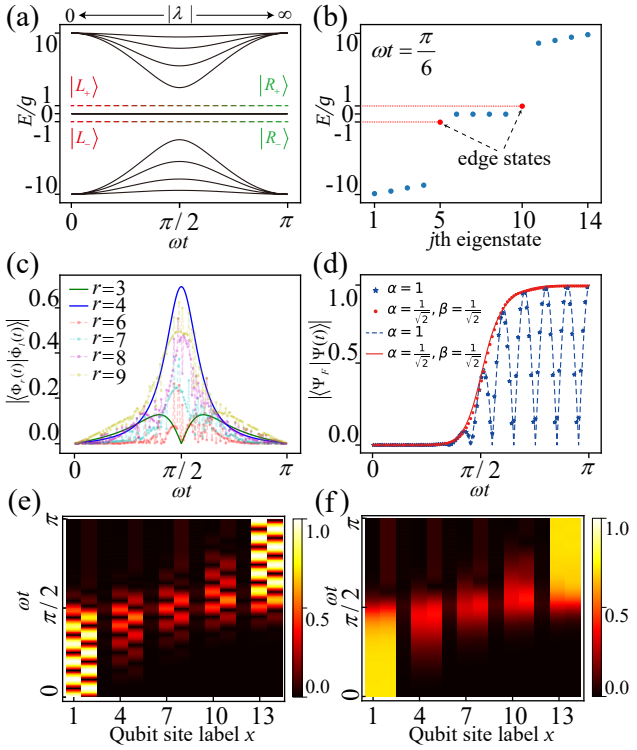

Figure 2. Two-qubit state transfer via a 14 qubits chain with 5 unit cells, i.e., $M = 5$. The system parameters are $J = 5g$ and $g/2\pi = 10$MHz. (a) The energy spectrum for an extended SSH3 model. Black-solid lines represent the bulk states and color-dashed lines represent the edge states. Three bulk bands are divided by two edge states, the middle bulk is 4-fold degenerate. As ωt changes from 0 to π, edge states are transferred from the left end (red) to the right end (green). (b) Schematics for eigenstates distribution at $\omega t = \pi/6$. Each point represents one eigenstate. Blue and red dots represent bulk and edge states, respectively. (c) The variation of $|\langle\Phi_r(t)|\dot{\Phi}_l(t)\rangle|$ with the time evolution. Here $\Phi_l(t)$ takes the lower edge state, i.e., $l = 5$. (d) Time evolutions of the target state occupations $|\langle\Psi_F|\Psi(t)\rangle|$ for different initial states. Red-solid and blue-dashed curves denote theoretical solutions. Red dots and blue stars denote the numerical simulations. The red-solid curve and red dots correspond to the initial state $(|\mathcal{A}_{1,1}\rangle + |\mathcal{A}_{2,1}\rangle)/\sqrt{2}$. Meanwhile, the blue-dashed curve and blue stars correspond to the initial state $|\mathcal{A}_{1,1}\rangle$. (e) Time-dependent population distribution on each qubit in the chain when the initial state is prepared to single-qubit state $|\mathcal{A}_{1,1}\rangle$. (f) Time-dependent population distribution on each qubit in the chain when the initial state is prepared to two-qubit Bell state $(|\mathcal{A}_{1,1}\rangle + |\mathcal{B}_{2,1}\rangle)/\sqrt{2}$.

where $\theta(t) = -\int_0^t E(t')dt'$ is the dynamical phase and $r(t) = i\int_0^t \langle\Phi(t')|\dot{\Phi}(t')\rangle dt'$ is the geometric phase, which can be gauged out unless the evolution path is closed. The normalization of $|\Phi(t')\rangle$ implies that $\langle\Phi(t')|\dot{\Phi}(t')\rangle$ is imaginary, which guarantees that $r(t)$ is real [79]. In our protocol, with the chosen gauge as shown in Eq. (7), $|\Psi_\pm\rangle$ only contains real parameters along $\lambda(t) = [1-\cos(\omega t)]/[1+\cos(\omega t)]$, thus $\langle\Phi(t')|\dot{\Phi}(t')\rangle$ is real, which guarantees that $r(t)$ is imaginary. Therefore, the geometric phase $r(t)$ must be zero and is naturally gauged out.

We thus only need to consider the dynamical phase associated with the adiabatic process. If we adiabatically change the parameters v and w to the final time t, following the quantum adiabatic theorem, the initial state in Eq. (12) should evolve to the state

$$|\Psi(t)\rangle = \frac{\alpha+\beta}{\sqrt{2}}|\Psi_+(t)\rangle e^{-i\int_0^t E_+ dt'} + \frac{\alpha-\beta}{\sqrt{2}}|\Psi_-(t)\rangle e^{-i\int_0^t E_- dt'}. \quad (14)$$

As discussed above, $E_\pm$ in our model are both constants due to the nature of the topological edge state. As such the final state at the time t is

$$|\Psi(t)\rangle = \frac{\alpha+\beta}{\sqrt{2}}|\Psi_+(t)\rangle e^{-igt} + \frac{\alpha-\beta}{\sqrt{2}}|\Psi_-(t)\rangle e^{igt}. \quad (15)$$

Indeed, by solely observing the values of $E_\pm = \pm g$, we find that the phase factors e^{-igt} and e^{igt} for two involved edge states (from upper and lower branch respectively) have the same period $T = 2\pi/g$. Therefore, if the time evolution takes the dynamical period T, the dynamical phase difference between the two involved edge states in Eq. (15) will be zero. Hereafter, we name this dynamical period as an evolution cycle, which is different from the pumping cycle of Thouless pump, during which the center of mass of a state moves exactly the same number of unit cells as the system's Chern number [117–119]. In our case, the evolution cycle is to lift the concern of dynamical phases, which can be done by choosing the total adiabatic protocol time as a multiple of evolution cycles.

As shown in Fig. 2(a), if the control field applied to the coupling strength involves from $t_0 = 0$ to $t_f = \pi/\omega$, then the edge state is transferred from the left end to the right end. In this case, Eq. (15) becomes

$$|\Psi_f\rangle = \frac{\alpha+\beta}{\sqrt{2}}|R_+\rangle e^{-i\pi\frac{g}{\omega}} + \frac{\alpha-\beta}{\sqrt{2}}|R_-\rangle e^{i\pi\frac{g}{\omega}}. \quad (16)$$

Here we choose the evolution time t_f to be a multiple of evolution cycles, i.e., $t_f/T = g/2\omega = n$. n should be a large integer number to satisfy the adiabatic condition. Thus, the dynamical phases become zero and the state in Eq. (16) is involved to

$$|\Psi_F\rangle = \left(\alpha\sigma^+_{A_{1,M}} + \beta\sigma^+_{A_{2,M}}\right)|G\rangle. \quad (17)$$

Here, the subscript F denotes the state transferred perfectly, i.e., the final state. Therefore, an arbitrary two-qubit entangled state can be encoded by two edge states and perfectly transferred from the left end to the right end via an adiabatic passage. Notice that all along the protocol, only the $A_{1,m}$- and $A_{2,m}$-type qubits are occupied by the edge states, and the B_m-type qubits serve as the invariable medium. Thus the qubits $A_{1,m}$ and $A_{2,m}$

can be considered as the transport qubits, and the qubits B_m can be considered as the mediated qubits.

We here have two remarks. First, for the special case of two-qubit state transfer, the evolution time can be half of the evolution cycle defined above. In this case, the final state acquires a global phase factor -1, which does not affect the task of entangled state transfer. Second, one may worry about the robustness of such adiabatic protocol as we need a precise timing. This is unnecessary because along the way, the eigenvalues of the edge states are pinned at special constant values due to topological features and hence we still expect to have robust protocols.

C. Analysis on adiabatic condition and two examples of QST

We now analyze the condition of the adiabatic evolutions. The adiabatic approximation requires a small changing rate of the Hamiltonian $\dot{H}(t)$ and a large energy gap $|E_r - E_l|$ between the rth and lth eigenstates. For our protocol, if we assume that the lth eigenstate $|\Phi_l(t)\rangle$ is the edge state, then the adiabatic condition is given by

$$\left|\langle\Phi_r(t)|\dot{\Phi}_l(t)\rangle\right| = \left|\frac{\langle\Phi_r(t)|\dot{H}(t)|\Phi_l(t)\rangle}{E_r(t) - E_l(t)}\right| \ll 1, \quad (18)$$

where $E_r(t)$ is the instantaneous eigenenergy corresponding to the instantaneous state $|\Phi_r(t)\rangle$ for the time t. The eigenstates are sorted according to the corresponding eigenenergies (lowest to highest), and the 5th eigenstate in Fig. 2(a) is the lower edge state. Here we make the 14-qubit chain evolve 5 evolution cycles, i.e., $\omega = 0.1g$. As shown in Fig. 2(c), for the lower edge state ($l = 5$), the adiabatic conditions are checked to be satisfied with $r = 3, 4, 6, 7, 8, 9$. For the bulk state between two edge states ($r = 6, 7, 8, 9$), the results are not continuous due to the numerical instablity of degenerate eigensolutions of the system.

To interpret our protocol, we choose the final state occupation $|\langle\Psi_F|\Psi(t)\rangle|$ as the dynamical indicator. In Fig. 2(d), we compare the analytical and numerical results of this indicator. The analytical solution for $|\Psi(t)\rangle$ is given in Eq. (15), while the numerical solution is calculated with ordinary differential equation (ODE) solver for small and fixed step size. Here, $\omega = 0.1g$, and the evolving time is $t_f = 0.5\mu$s, i.e., exact 5 times of the dynamical period ($T = 2\pi/g = 0.1\mu s$). We typically choose two initial states to be transferred. The first one is single-qubit state

$$|\Psi_{\text{in}}^{(1)}\rangle = \sigma_{A_{1,1}}^{+}|G\rangle \equiv \frac{\sqrt{2}}{2}\left(|L_+\rangle + |L_-\rangle\right) \quad (19)$$

which can be obtained from Eq. (12) by setting $\alpha = 1$ and $\beta = 0$. The other one is two-qubit Bell state

$$|\Psi_{\text{in}}^{(2)}\rangle = \frac{\sqrt{2}}{2}\left(\sigma_{A_{1,1}}^{+} + \sigma_{A_{2,1}}^{+}\right)|G\rangle \equiv |L_+\rangle \quad (20)$$

with $\alpha = \beta = 1/\sqrt{2}$. For the first one of single-qubit state transfer, the analytical evolution of the state is given as

$$|\Psi^{(1)}(t)\rangle = \frac{\sqrt{2}}{2}\left(|\Psi_+\rangle e^{-igt} + |\Psi_-\rangle e^{igt}\right) \quad (21)$$

The analytical solution (blue-dashed line) and numerical simulation (blue stars) for the dynamical indicator $|\langle\Psi_F|\Psi(t)\rangle|$ are plotted as a function of the evolution time t in Fig. 2(d). In this case, the indicator $|\langle\Psi_F|\Psi(t)\rangle|$ has a periodic variation due to the dynamical phase difference between the two edge states. The analytical result agrees well with numerical one, this confirms that the chosen parameters have fulfilled the adiabatic conditions. For two-qubit Bell state transfer, the adiabatic evolution of the state is

$$|\Psi^{(2)}(t)\rangle = |\Psi_+\rangle e^{-igt}. \quad (22)$$

In this case, the dynamical phase can be gauged out as one global phase, so the dynamical indicator does not oscillate and increases smoothly with the time. Again, the analytical result (red line) agrees well with numerical (red dots) one.

The first case for single-qubit state transfer of Eq. (21) is further analyzed in Fig. 2(e), where we show the population distribution $|\langle P_m|\Psi^{(1)}(t)\rangle|$ ($P_m \in \{|\mathcal{A}_{1,m}\rangle, |\mathcal{A}_{2,m}\rangle, |\mathcal{B}_m\rangle\}$) on each site of the state $|\Psi^{(1)}(t)\rangle$ during the adiabatic protocol. The state distribution shifts from the left to the right with rapid oscillations, due to coherent effect caused by the dynamical phase difference between the two involved edge states as mentioned above. However, for the second case shown in Eq. (22), Fig. 2(f) demonstrates the smooth transfer of the state $|\Psi^{(2)}(t)\rangle$ without any oscillation.

D. Robustness analysis for two-qubit state transfer

Any realistic implementation of the theoretical protocol unavoidably involves disorders from many aspects, e.g., the environmental effect, the time inaccuracy of the control field applied for the adiabatic evolution, nonuniform of the prepared qubits and imprecise couplings between the qubits in the chain. Here, we consider two main imperfections: one is the disorder of the qubit couplings and the other one is inaccuracy of the evolution time to achieve perfect state transfer.

The first kind of the disorders can be analyzed by modelling it as external perturbation terms in our system

Hamiltonian, i.e.,

$$\delta H = \sum_{m=1}^{M-1} \left(\delta\mu_{A_{1,m}} \sigma^{+}_{A_{1,m}} \sigma^{-}_{B_m} + \delta\mu_{B_m} \sigma^{+}_{A_{1,m+1}} \sigma^{-}_{B_m} + \text{H.c.} \right) + \sum_{m=1}^{M} \left(\delta\mu_{A_{2,m}} \sigma^{+}_{A_{1,m}} \sigma^{-}_{A_{2,m}} + \text{H.c.} \right), \quad (23)$$

where $\delta\mu_{A_{1,m}}$, $\delta\mu_{A_{2,m}}$, and $\delta\mu_{B_m}$ are the disorder coefficients, and assumed to satisfy the the Gaussian distribution as $\sim \exp[(-\delta\mu)^2/2\xi^2]$, with ξ being the standard deviation of the disorder in the coupling strength, i.e., the coupling disorder strength. Note that all these disorders are related to the control field. Thus, with the variation of the adiabatic parameters, it is more realistic to assume these disorders to be time-dependent, i.e., the temporal noises. If the initial state is prepared to $|\Psi_{\text{in}}\rangle = \left(\alpha\sigma^{+}_{A_1,1} + \beta\sigma^{+}_{A_2,1}\right)|G\rangle$, then the adiabatic evolution can be derived as

$$|\psi(t)\rangle = U(t)\,|\Psi_{\text{in}}\rangle = \mathcal{T} e^{-i\int_0^t H(t') + \delta H(t') dt'} |\Psi_{\text{in}}\rangle, \quad (24)$$

where $\mathcal{T}$ is the time order operator. The numerical simulation of this process can be written as $U(t) = \mathcal{T}\prod e^{-i[H(t')+\delta H(t')]\Delta t}$ ($\Delta t \ll T$). When $t = t_f$, the state described in Eq. (24) evolves to $|\psi_f\rangle$. Thus, the fidelity is given as

$$F = |\langle\Psi_F|\psi_f\rangle|, \quad (25)$$

where $|\Psi_F\rangle$ is the perfectly transferred state given in Eq. (17).

To verify the protocol robustness against these disorders, we first determine the proper evolution cycles n under the ideal condition without disorder. As shown in Fig. 3(a), we have numerically calculated the fidelity F given in Eq. (25) for the right edge state transferred with different evolution cycles and different lengths of the chain. These results help us to determine what extent we are working in the adiabatic regime. Indeed, the fidelity rises rapidly with the increases in the number of evolution cycles. As shown in Fig. 3(a), when the number of unit cells of the chain varies from 2 to 8, the necessary numbers of evolution cycles to achieve good fidelity increase from 5 to 10. Therefore, to guarantee the adiabatic condition and obtain good fidelity for the transferred state, we choose $n = 10$ as the number of evolution cycles for the following discussions, i.e., $t_f = 10\,T = 1\mu s$.

In our numerical simulations, we do 100 repetitions of the adiabatic evolution for a given time t_f, and each repetition has its different random choice of disorder. We here consider the average fidelity $\mathcal{F} = \overline{F}$ over these 100 calculations. In Fig. 3(b), we plot the distribution of fidelities for 100 repetitions of one chosen state transfer protocol. Here, the number of unit cells is taken as $M = 4$, and the coupling disorder strength ξ is taken as $\xi = 0.5g$. The distribution of fidelities for each simulation run is highly concentrated around the average fidelity, so the average fidelity here is a proper representation for the protocol fidelity.

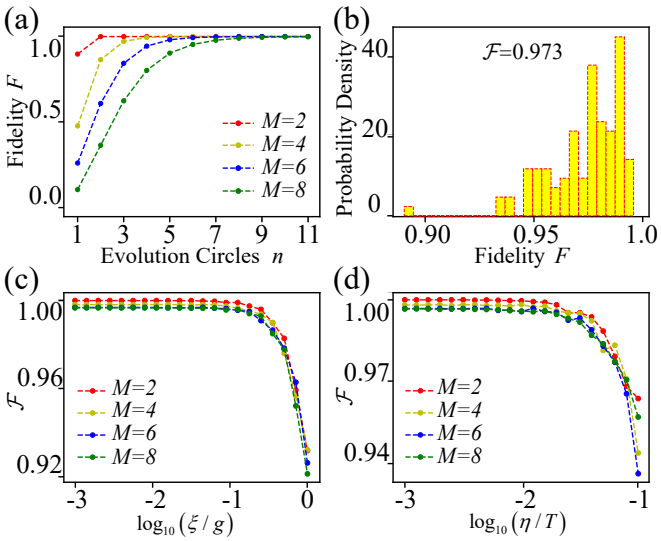

Figure 3. Robustness of our protocol for two-qubit state transfer. (a) The right edge target-state occupations (fidelity F) with different evolving cycles. As the qubit number of the chain becomes larger, the evolving cycles demanded for the adiabatic evolution increase from 5 to 10. For a qubit chain containing 23 qubits, i.e., 8 unit cells, it needs at least 10 evolving cycles to guarantee the adiabaticity. (b) The distribution of fidelities for one settled state transfer process with 100 repetitions where $\xi = 0.5g$ and $M = 4$. (c) The average fidelities of two-qubit entangled state transfer with the coupling disorder. The numbers of unit cells are 2, 4, 6, and 8 for each curve, separately. (d) The average fidelities of two-qubit entangled state transfer with the imperfection of the evolution time.

In Fig 3(c), the effect of the coupling disorder on the protocol fidelities is shown for different lengths of the chain, i.e., $M = 2, 4, 6, 8$, respectively. For each length of the chain, we find that the average fidelity $\mathcal{F}$ for 100 repetition calculations decreases from 1 to 0.92, as the coupling disorder strength ξ changes from $10^{-3}g$ to g. We also find that there is a plateau near $\mathcal{F} = 1$ for each case when ξ is taken from the range $\xi \in [10^{-3}g, 10^{-1}g]$. Therefore, for our protocol, the fidelity $\mathcal{F}$ will remain above 99% as long as the coupling disorder strength ξ is less than $0.1g$, which should be experimentally accessible.

The second kind of the disorders is the inaccuracy of protocol execution time. Unlike a usual adiabatic process, our protocol demands the total evolution time be exact multiple of the dynamical period. However, the control inaccuracy for the evolution time may lead to the imperfection of the target state. This kind of imperfection can be examined by an external perturbation time δt, which satisfies the Gaussian distribution as $\delta t \sim \exp[(-\delta t)^2/2\eta^2]$. η is the standard deviation of the evolution time. In this case, the modified transferred

state can be derived as

$$|\psi_f\rangle = U\left(t_f+\delta t\right)|\Psi_{\rm in}\rangle = \mathcal{T}e^{-i\int_0^{t_f+\delta t}H(t')dt'}|\Psi_{\rm in}\rangle, \quad (26)$$

with the time inaccuracy δt. Figure 3(d) depicts the impact of the evolution time imperfection. We find that the average fidelity $\mathcal{F}$ for each chain decreases from 1 to 0.94 as the time disorder strength η changes from $10^{-3}T$ to $10^{-1}T$. For our protocol, the fidelity will remain above 99% when the time disorder strength η is less than $0.01T$.

Therefore, we conclude that our protocol is robust against both the qubit coupling disorder and the inaccuracy of the protocol execution time.

IV. EXTENDED PROTOCOLS FOR $\mathcal{N}$-QUBIT STATE TRANSFER

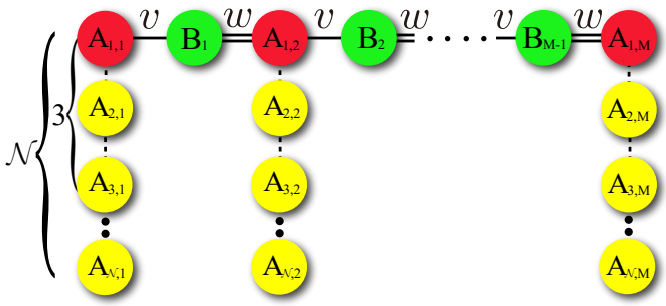

Figure 4. Schematic of the extended SSH chain for 3-qubit and $\mathcal{N}$-qubit state transfer. Each unit cell hosts 4 to $\mathcal{N}+1$ qubits. The edge states are localized among the transport qubits from $A_{1,m}$ to $A_{\mathcal{N},m}$ with $m=1,\cdots,M$. The rest qubits are mediated qubits labeled as B_m with $m=1,\cdots,M-1$. v denotes the coupling between qubits $A_{1,m}$ and B_m, w denotes the coupling between qubits $A_{1,m+1}$ and B_m.

Our protocol for arbitrary two-qubit entangled state transfer through extended SSH chain can be easily generalized to $\mathcal{N}$-qubit state transfer. For $\mathcal{N}$-qubit transfer process, as schematically shown in Fig. 4, the extended SSH model has $\mathcal{N}+1$ sites ($\mathcal{N}$ transport qubits and 1 mediated qubit) in each unit cell, and the whole qubit chain with M unit cells has $\mathcal{L}=(\mathcal{N}+1)M-1$ qubits. With the increase of the site number in each unit cell, more edge states emerge. Thus it is not an easy task to find a proper evolution time to cancel all dynamical phase differences between these edge states in our protocol. As such, the couplings between the transport qubits should not simply be the constant g. To this end, we may consider the following modified Hamiltonian

$$\begin{aligned} H=&\sum_{m=1}^{M-1}\left(v\sigma_{A_{1,m}}^{+}\sigma_{B_m}^{-}+w\sigma_{A_{1,m+1}}^{+}\sigma_{B_m}^{-}+\text{H.c.}\right)\\ &+\sum_{m=1}^{M}\left(g_1\sigma_{A_{1,m}}^{+}\sigma_{A_{2,m}}^{-}+g_2\sigma_{A_{2,m}}^{+}\sigma_{A_{3,m}}^{-}+\cdots\right.\\ &\left.+\ g_{\mathcal{N}-1}\sigma_{A_{\mathcal{N}-1,m}}^{+}\sigma_{A_{\mathcal{N},m}}^{-}+\text{H.c.}\right). \end{aligned} \quad (27)$$

In each unit cell, these $\mathcal{N}$ transport quibts form an array with coupling constants $g_1,\cdots,g_{\mathcal{N}-1}$, and all of the mediated qubits B_m are used to couple the arrays of transport qubits with coupling constants v and w, respectively.

Analogously, we can extend our proposal from 2-qubit state transfer to $\mathcal{N}$-qubit state case. Similar to Eq. (3) for the two-qubit entangled state transfer, the edge states corresponding to the Hamiltonian in Eq. (27) do not occupy the mediated qubits B and can be expanded as

$$|\Psi_{\rm edge}\rangle=\sum_{m=1}^{M}\lambda^m\left(\chi_1\sigma_{A_{1,m}}^{+}+\cdots+\chi_{\mathcal{N}}\sigma_{A_{\mathcal{N},m}}^{+}\right)|G\rangle. \quad (28)$$

Substituting Eq. (27) and Eq. (28) into the Schrödinger equation $H|\Psi_{\rm edge}\rangle=E|\Psi_{\rm edge}\rangle$, then we can have

$$\begin{aligned} &E\left(\chi_1\sigma_{A_{1,m}}^{+}+\chi_2\sigma_{A_{2,m}}^{+}+\cdots+\chi_{\mathcal{N}}\sigma_{A_{\mathcal{N},m}}^{+}\right)|G\rangle\\ &=\left(g_1\chi_2\sigma_{A_{1,m}}^{+}+\cdots+g_{\mathcal{N}-1}\chi_{\mathcal{N}}\sigma_{A_{\mathcal{N}-1,m}}^{+}\right)|G\rangle\\ &+\left(g_1\chi_1\sigma_{A_{2,m}}^{+}+\cdots+g_{\mathcal{N}-1}\chi_{\mathcal{N}-1}\sigma_{A_{\mathcal{N},m}}^{+}\right)|G\rangle\\ &+\chi_1\left(v\sigma_{B_m}^{+}+w\lambda\sigma_{B_m}^{+}\right)|G\rangle. \end{aligned} \quad (29)$$

From Eq. (29), it is straightforward to get $\lambda=-v/w$, and the coefficients $\chi_1,\chi_2,\cdots,\chi_{\mathcal{N}}$ satisfy the following equation

$$\begin{pmatrix} 0 & g_1 & 0 & 0 & 0\\ g_1 & 0 & g_2 & 0 & 0\\ 0 & g_2 & 0 & \ddots & 0\\ 0 & 0 & \ddots & \ddots & g_{\mathcal{N}-1}\\ 0 & 0 & 0 & g_{\mathcal{N}-1} & 0 \end{pmatrix}\begin{pmatrix}\chi_1\\ \chi_2\\ \chi_3\\ \vdots\\ \chi_{\mathcal{N}}\end{pmatrix}=E\begin{pmatrix}\chi_1\\ \chi_2\\ \chi_3\\ \vdots\\ \chi_{\mathcal{N}}\end{pmatrix}. \quad (30)$$

Solving this eigen-equation, we can obtain the eigenenergies of the edge states as $E_1,\cdots,E_{\mathcal{N}}$. The explicit eigenstates can also be derived, and then edge states can be obtained. Similar to Eq. (10), when the time t is adiabatically changed from 0 to π/ω, the coupling constant v (w) is changed from $2J$ (0) to 0 ($2J$), and the edge states initially at the left end of the chain can be adiabatically transferred to the right end. We know that an arbitrary $\mathcal{N}$-qubit entangled state can be represented by these edge states, thus $\mathcal{N}$-qubit entangled state can also be perfectly transferred from the left end to the right end of the chain if the total evolution time $t_f=\pi/\omega$ is exact multiple of all the dynamical periods corresponding to all eigenenergies $E_1,\cdots,E_{\mathcal{N}}$. That is,

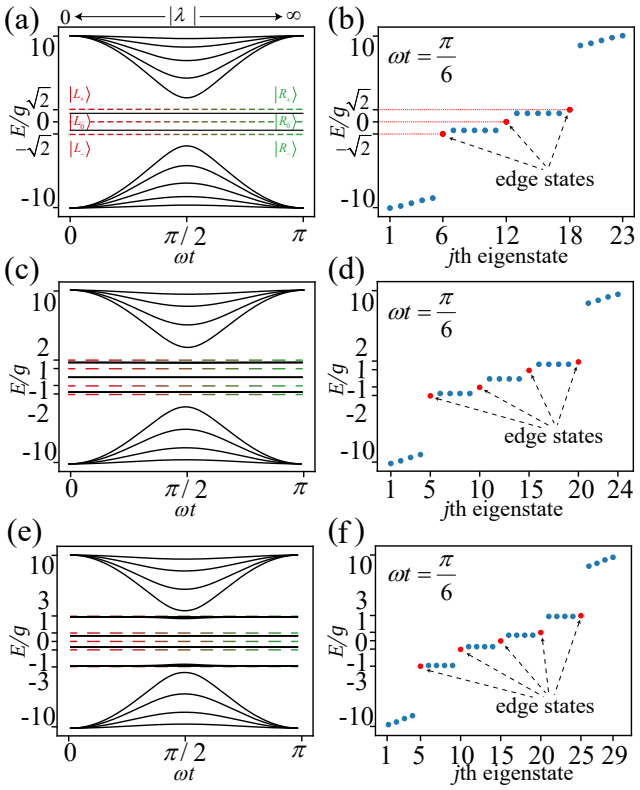

Figure 5. The energy spectrums of the qubit chain when ωt changes from 0 to π. Edge states can be transferred from left edge (red) to right edge (green) along the dashed energy levels. (a) Spectrum of the qubit chain for 3-qubit state transfer. Here, $M = 6$ and $\mathcal{L} = 23$. The color-dashed lines represent the edge states and the black-solid lines represent the bulk states. (b) Schematics for eigenstate distribution of the SSH4 chain in a topological nontrivial regime ($v \ll w$) when $\omega t = \pi/6$. Four bulk bands (blue dots), are divided by three edge states (red dots). (c) Spectrum of the qubit chain for 4-qubit state transfer. Here, $M = 5$ and $\mathcal{L} = 24$. The color-dashed lines represent the edge states and the black-solid lines represent the bulk states. (d) Schematics for eigenstates distribution corresponding to (c) in a topologically nontrivial regime ($v \ll w$) when $\omega t = \pi/6$. Four red dots denote four edge states. The blue dots denote the bulk bands. The four blue dots in line between two red dots denote a bulk band with 4-fold degenerate. (e) Spectrum of the qubit chain for 5-qubit state transfer. Here, $M = 5$ and $\mathcal{L} = 29$. (f) Schematics for eigenstates distribution corresponding to (e) in a topologically nontrivial regime ($v \ll w$) when $\omega t = \pi/6$. Five red dots denote five edge states. The blue dots denote the bulk bands. The four dots in line between two red dots denote a bulk band with 4-fold degenerate.

there must be a least common period of all dynamical periods $T_1 = 2\pi/E_1, \cdots, T_{\mathcal{N}} = 2\pi/E_{\mathcal{N}}$ corresponding to the $\mathcal{N}$ edge states. This common period can only exist for specific set of parameters $\{g_1, \cdots, g_{\mathcal{N}-1}\}$.

It seems that the generalization is straightforward, however the main problem is how to engineer the proper series of parameters $\{g_1, \cdots, g_{\mathcal{N}-1}\}$ to get a common period. It is highly challenging to find a general solution for any $\mathcal{N}$, because the solution varies case by case. However, for given qubit states, we can always engineer the coupling constants between the transport qubits such that these states can be transferred through the extended SSH chain. Below, three examples for $\mathcal{N} = 3, 4, 5$ are further shown in Fig. 5. For $\mathcal{N} = 3$, the parameters $\{g_1, g_2\}$ can be set as $g_1 = g_2 = g$ and the corresponding eigenenergies are $\{\sqrt{2}g, -\sqrt{2}g\}$. In Figs. 5(a) and (b), we show the spectrum of the qubit chain for 3-qubit state transfer with a number of 23 qubits. Four bulk bands are divided by three edge states, and the two bulk bands between edge states are 5-fold degenerate. The least common oscillation period of these edge states is $\sqrt{2}\pi/g$, which can be taken as the ideal time evolution cycle. This particular case for 3-qubit QST is exhaustively discussed in Appendix D. For $\mathcal{N} = 4$, the parameters $\{g_1, g_2, g_3\}$ can be set as $\{\sqrt{2}g, g, \sqrt{2}g\}$ and the corresponding eigenenergies are $\{2g, g, -g, -2g\}$. In Figs. 5(c) and (d), we show the spectrum of the qubit chain for 4-qubit state transfer with a number of 24 qubits. Five bulk bands are divided by four edge states, and the three bulk bands between edge states are 4-fold degenerate. The least common oscillation period of these edge states is $2\pi/g$. For $\mathcal{N} = 5$, the parameters $\{g_1, g_2, g_3, g_4\}$ can be set as $\{g, 2g, 2g, g\}$ and the corresponding eigenenergies are $\{3g, g, 0, -g, -3g\}$. The spectrum of the qubit chain in this case is plotted in Figs. 5(e) and (f) for the total number 29 of the qubits in the chain. Six bulk bands are divided by five edge states, and the four bulk bands between edge states are 4-fold degenerate. The least common period is also $2\pi/g$. Similarly, for the case of $\mathcal{N}$-qubit state transfer, we can find a proper set of parameters to get a common period as the time evolution cycle. By use of such time evolution cycles, the involved edge states will not suffer from mutual dynamical phase differences at the end of our adiabatic protocol, and hence an arbitrary $\mathcal{N}$-qubit entangled state can be transferred from the left end to the right end.

V. DISCUSSIONS

A. General discussions

We have proposed a QST approach along an extended SSH qubit chain. However, several issues should be further discussed. First, we consider only the neighbor-couplings and on-site potentials are not included as shown in Eq. (1). This is because the on-site potentials only result in a global dynamical phase if all the qubits are tuned to resonate with each other, and thus this global phase can be dropped out. Second, we note that the gap between the edge states and the bulk states decreases with the increase in length of the qubit chain. This indicates that the adiabatic condition is highly demanded for very large systems. However, as shown by Fig. 10(c) in Appendix D, for an extended SSH4 chain

consisting of 8 unit cells, the adiabatic condition is still well met for an execution time of only 20 evolution cycles. Let us further discuss the adiabatic condition of a large system in our protocol. Using the extended SSH3 model as an example, the band gaps between the adiabatic passage and other bulk states are plotted in Fig. 6(a). The minimum evolution cycles $n_{\min}$ to execute adiabatic evolution are plotted in Fig. 6(b). Because the energy gap in Fig. 6(a) is plotted in log scale, the bending of the curve indicates a decrease slower than exponential decrease. After the number of unit cells M is larger than 100, the energy gap slowly approaches 10^{-3}. As shown in Fig. 6(b), the minimum evolution cycles increase from 3 to 50 as the number of unit cells changes from 2 to 16, and this is similarly not the exponential growth. When the length of the chain becomes much larger, one possible solution is hinted in Ref. [69]. That is, our QST protocol realized by one-step adiabatic evolution can be decomposed into multi-step process to achieve a better performance.

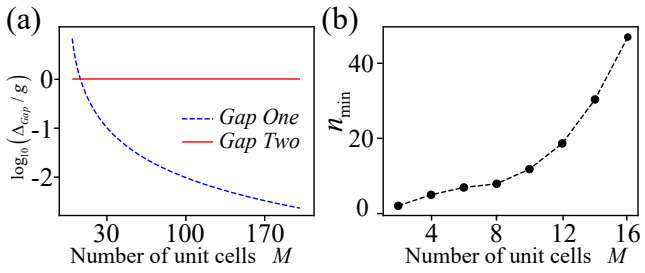

Figure 6. (a) The band gap between the edge states and bulk states changing with the system scale. The red-solid line represents the the energy gap between edge states and the middle bulk states, which as shown in Fig. 2(a) must be constant with the system scale. The blue-dashed line represents the energy gap between edge states and the upper or lower bulk states, which gets smaller with the system scale. (b) The minimum evolution cycles to execute perfect adiabatic evolution (Fidelity $F > 0.99$). Here we only exhibit the result for less than 16 unit cells restricted to the computational complexity.

To verify the topological protection of our QST protocol, one may compare our approach with QST protocols independent of topology. Using mirror symmetry, one can think of an obvious non-topological QST protocol in a qubit chain as follows. At the beginning, the leftmost qubit is decoupled from other part of the chain, and at the end the couplings of the qubit chain is slowly changed to the reversed form, i.e., the rightmost qubit is decoupled with other qubits. With this adiabatic process, the quantum state initially prepared to the leftmost qubit can be transferred from the left end to the right end. Ref. [93] has shown that such topologically-unrelated QST protocol is not robust to disorder. Hence, our topology-based protocol does have an advantage, accounting for the fairly good fidelity presented above in the presence of disorder.

Another well-known multi-step QST protocol is the Thouless pump [117]. For example, an array of nonlinear resonators formed of optical superlattices or circuit-QED architectures has been investigated to transfer Fock states [120] and bound bosonic pairs [121]. After each pumping cycle, the bound state prepared in the middle of the lattice can move across exactly one unit cell. This QST protocol utilizes bulk topological properties, and is very efficient and powerful as long as boundary effects are avoided. However, our QST protocol uses topological edge states to transfer quantum states, via edge state pumping. Our work is also different from a few other studies of topological pumping of quantum correlations [122, 123]. There the pumping protocols may be achieved by mapping some highly correlated states to uncorrelated ones and the entanglement of these correlated states can be strongly modified during the pumping process. By contrast, our edge state pumping protocol can, in principle, perfectly transfer a class of entangled states by use of a superposition of topological edge states.

B. Discussions for implementations using superconducting qubit circuits

In principle, our proposal can be implemented in various platforms, e.g., cold atoms [124], trapped ions [125], or coupled waveguides [126, 127]. However, with the significant development in recent years, superconducting qubit circuits, e.g., transmon or Xmon qubits [99], seem to be a more promising platform [128]. Also, a fast and high-fidelity transfer of arbitrary single-qubit state in a chain of superconducting qubits has been achieved in experiment recently [129].

The good scalability and flexible tunability for the couplings make our extended SSH chain easy to be realized by the superconducting qubit circuits. In particular, the coupling strengths can be tuned from topologically trivial to non-trivial regime. Thus topological and non-topological phenomena can be studied in one quantum circuits. Moreover, the coherent time is a very important for realizing our proposal. As shown in Appendix A, the coupling coefficient g can be chosen as $g/2\pi = 10$Mhz by using the parameters of current superconducting qubit circuits for realizing our proposal. Therefore, for two-qubit state transfer, one evolution cycle can be $T = 2\pi/g = 0.1\mu s$. The total evolution time is 10 evolution cycles, i.e., $t_f = 1\mu s$. For three-qubit state transfer, one evolution cycle can be $T = 2\pi/\sqrt{2}g = 0.0707\mu s$. The total evolution time is 20 evolution cycles, i.e., $t_f = 1.414\mu s$. In superconducting qubit circuits, the coherence time of single qubit is about $10 \sim 100\mu s$ [97, 98], which is much longer than the adiabatic time in our proposal. Meanwhile, steady topological edge states have already been observed in superconducting qubit circuits, which can last more than $1\mu s$ [105]. Therefore, the decoherence effect is not expected to be troublesome in our protocol.

To make sure that the adiabatic evolution time for our proposal is indeed integral multiple of the evolution cy-

cle, one needs to measure the exact value of g, which is equivalent to determining the eigenenergy of edge states. This can be achieved by the reflection spectrum of a weak probe light through a waveguide coupled to the extended SSH chain (see Appendix E). The reflection peaks of the input weak signal can reveal the energy spectrum of the qubit chain with appropriate parameters, and the value of coupling g can be obtained with the energy shift between the edge states.

VI. CONCLUSION

In summary, we have proposed an experimentally feasible approach for transferring arbitrary entangled state through an extended SSH chain. The entangled states are encoded in the edge states of a class of extended SSH chains, and then they are transported via an adiabatic protocol. Due to the topological protection of the edge states, our protocol is robust against the the temporal noise caused by the imperfection in the control field. We have numerically confirmed this robustness against two kinds of disorders, i.e, the coupling strength disorder and the execution time disorder. Compared with most contemporary studies realizing QST in qubit chains, this work represents an exciting advance that a general scenario is proposed to achieve QST of arbitrary $\mathcal{N}$-qubit entangled state. Our proposal is easy to be realized by using superconducting qubit circuits and the parameters required in our protocol are estimated according to the recent experiments. Given the feasibility and tunability of the proposed protocal, our idea can also be extended for realizing QST in two dimensional quantum networks.

VII. ACKNOWLEDGMENTS

We thank Wei Nie for helpful discussions. Y.X.L. is supported by the Key-Area Research and Development Program of GuangDong Province under Grant No. 2018B030326001, the National Basic Research Program (973) of China under Grant No. 2017YFA0304304, and the NSFC under Grant No. 11874037. J.G. acknowledges funding support by the Singapore NRF Grant No. NRF NRFI2017-04 (WBS No. R-144-000-378- 281).

Appendix A: Xmon qubit chain with tunable couplings

For our state transfer protocol, the feasibility comes from the precise tuning of the coupling between qubits in the topological qubit chain. We manage to realize such setup with superconducting qubits. A superconducting qubit chain with tunable couplings is presented in Fig. 1(a). The details of the coupler circuit are schematically shown in Fig. 1(b), where two Xmon qubits are coupled by a tunable Josephson junction coupler. Such coupling scheme has been experimentally realized in Ref. [99] and theoretically analyzed in Ref. [100].

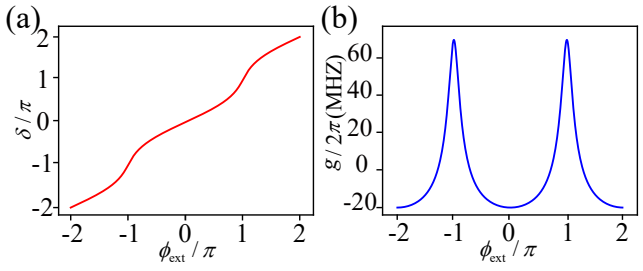

Figure 7. (a) The change of δ versus $\phi_{\rm ext}$. The parameters we use here are $L_{\rm g} = 300$ pH and $L_{\rm T} = 1$ nH. (b) Coupling strength varies with $\phi_{\rm ext}$. The parameters are $L_{\rm J} = 8$ nH and $\omega_q = 5.5$ GHz. Other parameters are the same as above.

The junction connecting two qubits provides a tunable effective inductance $L_{\rm eff}$ to tune the coupling, and a magnetic flux bias $\Phi_{\rm ext}$ is used to tune the coupler's effective inductance $L_{\rm eff} = L_{\rm T}/\cos\delta$ [100], where δ is the phase difference across the coupler. For the coupler loop, we have $\Phi = (\Phi_0/2\pi)\delta$, where Φ is the total magnetic flux and $\Phi_0 = h/2e$. $L_{\rm T} = \Phi_0/2\pi I_c$ is the zero-bias inductances of the Josephson coupler and I_c is the critical current of the coupler junction. The circuit flux has the relation $\Phi = \Phi_{\rm ext} - 2L_{\rm g}I_c\sin\delta$ and therefore we can have

$$\phi_{\rm ext} = \delta + \left(\frac{2L_{\rm g}}{L_{\rm T}}\right)\sin\delta \tag{A1}$$

where $\phi_{\rm ext} = 2\pi\Phi_{\rm ext}/\Phi_0$. In the the weakly coupled limit the effective coupling strength is approximately [99]

$$g = -\frac{\omega_q}{2}\frac{M}{L_{\rm J}+L_{\rm g}}, \tag{A2}$$

where $M = L_{\rm g}^2/(2L_{\rm g}+L_{\rm eff})$ is the mutual inductance and ω_q is the qubit frequency. Thus the coupling strength can be finally given by [100]

$$g = -\frac{L_{\rm g}^2\cos\delta}{2\left(L_{\rm J}+L_{\rm g}\right)\left(L_{\rm T}+2L_{\rm g}\cos\delta\right)}\omega_q. \tag{A3}$$

In Fig. 7(a), we present the relation between $\Phi_{\rm ext}$ and δ. The phase δ can be tuned from -2π to 2π when the external magnetic flux $\Phi_{\rm ext}$ is continuously changed. In Fig. 7(b), we show how the coupling between qubits can be tuned with $\Phi_{\rm ext}$. As $\phi_{\rm ext}$ is changing from -2π to 2π, the coupling can be tuned from -20MHZ to 60MHZ, which meet the requirement of the system parameters to realize our proposal.

Appendix B: A straightforward diagram for exact solution of the edge states

As for standard SSH model, there are only approximated solutions for hybridized edge states [82], but for

our imperfect SSH model, one can obtain the exact solution of the edge states [55]. To illustrate this process straightforwardly, let us rewrite the qubit array with specific set of basis. As shown in Fig. 1, we here analyze 2-qubit state transfer, and the formula can be extended to 3-qubit and $\mathcal{N}$-qubit cases.

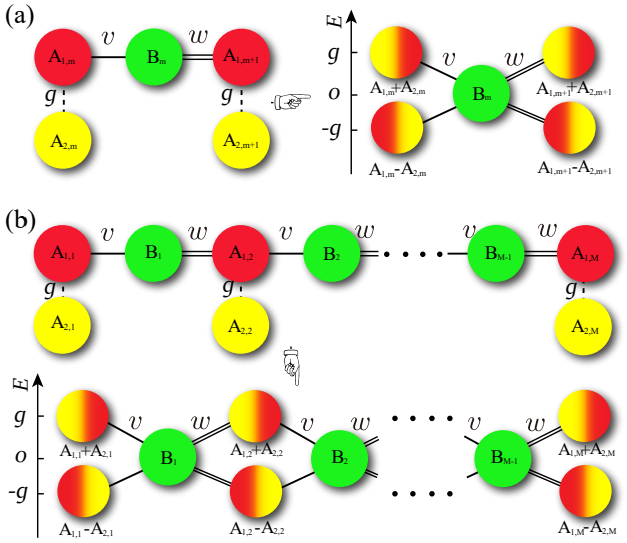

Figure 8. Schematic diagram of the renormalization process on qubit array with orthogonal basis of transport qubits. (a) For each unit cell of the qubit chain, the renormalization leads to two on-site potentials as g and $-g$, due to the coupling strength g between the transport qubits $A_{1,m}$ and $A_{2,m}$. (b) Renormalization of the whole qubit array. All the transport qubits are decoupled with each other, and the hopping amplitudes are staggered through the mediated qubits B_m. The qubit array now can be distinguished into two branches by the on-site energy: the upper branch with the hybrid qubit $A_{1,m}+A_{2,m}$ and the lower branch with the hybrid qubit $A_{1,m}-A_{2,m}$.

For 2-qubit state transfer, the Hamiltonian of the qubit chain is

$$H=\sum_{m=1}^{M-1}\left(v\sigma_{A_{1,m}}^{+}\sigma_{B_m}^{-}+w\sigma_{A_{1,m+1}}^{+}\sigma_{B_m}^{-}+\text{H.c.}\right)+\sum_{m=1}^{M}\left(g\sigma_{A_{1,m}}^{+}\sigma_{A_{2,m}}^{-}+\text{H.c.}\right), \tag{B1}$$

same as Eq. (1). As shown in Fig. 8(a), for a single unit cell of the qubit chain, the Hamiltonian is

$$H_{\text{cell}}=v\sigma_{A_{1,m}}^{+}\sigma_{B_m}^{-}+w\sigma_{A_{1,m+1}}^{+}\sigma_{B_m}^{-}+\text{H.c.}+g\sigma_{A_{1,m}}^{+}\sigma_{A_{2,m}}^{-}+g\sigma_{A_{1,m+1}}^{+}\sigma_{A_{2,m+1}}^{-}+\text{H.c.}. \tag{B2}$$

In the single-excitation subspace, the Hamiltonian in Eq.(B2) can be rewritten as

$$H_{\text{cell}}=v|\mathcal{A}_{1,m}\rangle\langle\mathcal{B}_m|+w|\mathcal{A}_{1,m+1}\rangle\langle\mathcal{B}_m|+\text{H.c.}+g|\mathcal{A}_{1,m}\rangle\langle\mathcal{A}_{2,m}|+g|\mathcal{A}_{1,m+1}\rangle\langle\mathcal{A}_{2,m+1}|+\text{H.c.}. \tag{B3}$$

The term of $g|\mathcal{A}_{1,m}\rangle\langle\mathcal{A}_{2,m}|+\text{H.c.}$ in matrix form is $\begin{pmatrix}0&g\\g&0\end{pmatrix}$, and can be renomorlized as $\begin{pmatrix}g&0\\0&-g\end{pmatrix}$ with basis of $|\chi_{m,+}\rangle=\left(|\mathcal{A}_{1,m}\rangle+|\mathcal{A}_{2,m}\rangle\right)/\sqrt{2}$ and $|\chi_{m,-}\rangle=\left(|\mathcal{A}_{1,m}\rangle-|\mathcal{A}_{2,m}\rangle\right)/\sqrt{2}$. In the basis $\{|\chi_{m,+}\rangle,|\chi_{m,-}\rangle,|\mathcal{B}_m\rangle\}$, the Hamiltonian H_{cell} of the single unit cell can be rewritten as

$$\begin{aligned}H_{\text{cell}}^{R}=&\,v\frac{|\chi_{m,+}\rangle+|\chi_{m,-}\rangle}{\sqrt{2}}\langle\mathcal{B}_m|+\text{H.c.}\\&+w\frac{|\chi_{m+1,+}\rangle+|\chi_{m+1,-}\rangle}{\sqrt{2}}\langle\mathcal{B}_m|+\text{H.c.}\\&+g|\chi_{m+1,+}\rangle\langle\chi_{m+1,+}|-g|\chi_{m+1,-}\rangle\langle\chi_{m+1,-}|\\&+g|\chi_{m,+}\rangle\langle\chi_{m,+}|-g|\chi_{m,-}\rangle\langle\chi_{m,-}|.\end{aligned} \tag{B4}$$

The coupling between $A_{1,1}$ and $A_{2,1}$ in the unit cell leads to two on-site potentials g and $-g$. The total Hamiltonian of the qubit chain in such new basis is

$$\begin{aligned}H^{R}=&\sum_{m=1}^{M-1}\left(v\frac{|\chi_{m,+}\rangle+|\chi_{m,-}\rangle}{\sqrt{2}}\langle\mathcal{B}_m|+\text{H.c.}\right)\\&+\sum_{m=1}^{M-1}\left(w\frac{|\chi_{m+1,+}\rangle+|\chi_{m+1,-}\rangle}{\sqrt{2}}\langle\mathcal{B}_m|+\text{H.c.}\right)\\&+\sum_{m=1}^{M}g\left(|\chi_{m,+}\rangle\langle\chi_{m,+}|-|\chi_{m,-}\rangle\langle\chi_{m,-}|\right).\end{aligned} \tag{B5}$$

That is, as shown in Fig. 8(b), the renormalized qubit chain can be divided into two different branches by on-site potential. The upper branch's transport qubits now are $A_{1,m}+A_{2,m}$ and lower branch's transport qubits are $A_{1,m}-A_{2,m}$. Two branches have the same mediated qubits B_m. The edge states for the upper and lower branches can be written as

$$\begin{aligned}|\Psi_{\pm}\rangle=&\sum_{m=1}^{M}\lambda^{m}|\chi_{m,\pm}\rangle\\=&\sum_{m=1}^{M}\lambda^{m}\left(\frac{|\mathcal{A}_{1,m}\rangle\pm|\mathcal{A}_{2,m}\rangle}{\sqrt{2}}\right),\end{aligned} \tag{B6}$$

which is the same as Eq. (7). The extension of this analysis for 3-qubit and $\mathcal{N}$-qubit state transfer is straightforward, thus we will not elaborate here.

Appendix C: Topological invariant for our extended SSH model

In the standard SSH model with an even number of qubits, edge states appear when the coupling strength at

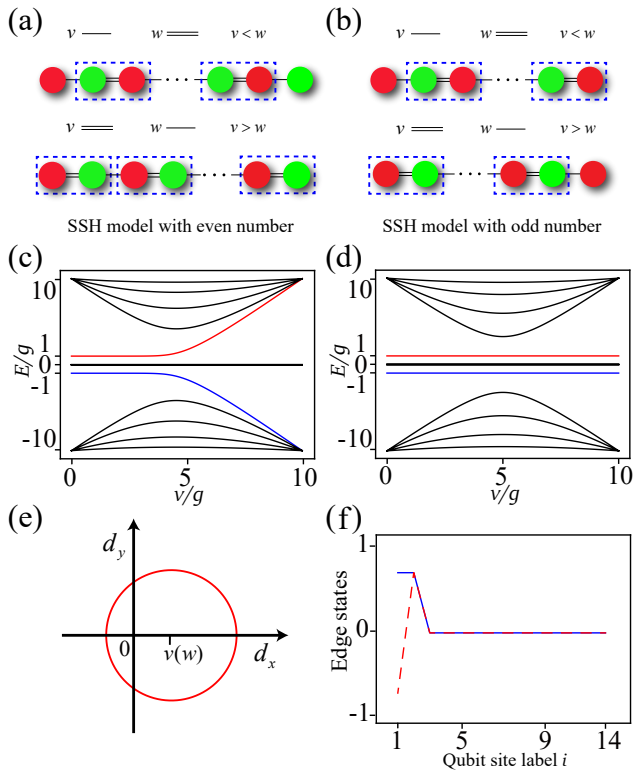

Figure 9. Topological invariant and edge states for our extended SSH model. (a) SSH model with an even number of qubits. When $v < w$, the qubits at two end are insulated and edge states appear. When $v > w$, all qubits are included in bulk states and edge states disappear. (b) SSH model with an odd number of qubits. we can see the system always has an edge state whether if $v < w$ or $v > w$. (c) Energy spectrum for extended SSH model with complete $3M$ qubits. Two edge states are denoted with blue- and red- lines. Topological phase transition occurs with the increasing of v, and edge states join the bulk band when $v \gg w$. (d) Energy spectrum for our extended SSH model with $3M-1$ qubits, i.e., lacking of one qubit at the right end of the chain. The system always has two edge states with the variation of couplings. (e) Winding number in d_x-d_y plane. When $v < w$ ($v > w$), the centre of the integral cycle is located at v (w) on d_x axis. (f) Edge states for our extended SSH model, i.e., $(|\mathcal{A}_{1,1}\rangle \pm |\mathcal{A}_{2,1}\rangle)/\sqrt{2}$.

the edge is weaker than the coupling at bulk. As shown in Fig. 9(a), if $v < w$, the qubits at two ends are isolated from bulk and form two edges. If $v > w$, all qubits are included in bulks. For our extended SSH3 model, with $g = 0$, sublattices $A_{1,m}$ and B_m are decoupled from $A_{2,m}$, forming the SSH model with an odd number of qubits. The Hamiltonian of such SSH model is ($A_{1,m}$ is redefined as A_m)

$$H_{\mathrm{SSH}} = \sum_{m=1}^{M-1} \left(v\sigma_{A_m}^{+}\sigma_{B_m}^{-} + w\sigma_{A_{m+1}}^{+}\sigma_{B_m}^{-} + \mathrm{H.c.} \right). \quad \text{(C1)}$$

As shown in Fig. 9(b), if $v < w$, the weaker coupling strength is v at the left edge. Otherwise, if $w < v$, the weaker coupling strength is w at the right edge.

For a standard SSH model which can be obtained by setting $g = 0$ of the SSH3 model, edge states are supported by the topological invariant defined in the phase space. We first assume $v < w$ and the unit cell is (A_m, B_m). Due to the translation invariance of the bulk, we can make Fourier transforms to the vectors $|\mathcal{A}_m\rangle$ and $|\mathcal{B}_m\rangle$ as

$$|\mathcal{A}_k\rangle = \frac{1}{\sqrt{M}} \sum_{m=1}^{M} e^{imk} |\mathcal{A}_m\rangle, \quad \text{(C2)}$$

$$|\mathcal{B}_k\rangle = \frac{1}{\sqrt{M}} \sum_{m=1}^{M} e^{imk} |\mathcal{B}_m\rangle, \quad \text{(C3)}$$

for $k \in \{\delta_k, 2\delta_k, \cdots, M\delta_k\}$ with $\delta_k = 2\pi/M$. Here k is the wavenumber of the first Brillouin zone [82]. The bulk momentum-space Hamiltonian $H(k)$ is defined as

$$H(k) = \sum_{\imath,\jmath \in \{\mathcal{A}_k, \mathcal{B}_k\}} \langle \imath | H_{\mathrm{SSH}} | \jmath \rangle |\imath\rangle\langle\jmath|. \quad \text{(C4)}$$

By choosing a fixed momentum k, we can get the matrix form of the bulk momentum-space Hamiltonian $h(k)$ as

$$h(k) = \begin{pmatrix} 0 & v + we^{-ik} \\ v + we^{ik} & 0 \end{pmatrix}. \quad \text{(C5)}$$

Thus the total Hamiltonian can be written as $H(k) = \sum_k \Psi_k^{\dagger} h(k) \Psi_k$, with $\Psi_k^{\dagger} = (|\mathcal{A}_k\rangle, |\mathcal{B}_k\rangle)$ and we have

$$h(k) = d_x(k)\sigma_x + d_y(k)\sigma_y, \quad \text{(C6)}$$

where $d_x(k) = v + w\cos k$, $d_y(k) = w\sin k$. The winding number as the topological invariant hence can be defined in d_x-d_y plane as

$$\mathrm{Winding} = \frac{1}{2\pi i} \int_{-\pi}^{\pi} \frac{d}{dk} \log \boldsymbol{h}(k), \quad \text{(C7)}$$

where $\boldsymbol{h}(k) = d_x(k) + id_y(k) = v + we^{ik}$.

Meanwhile, if $w < v$, the unit cell is (B_m, A_{m+1}). Thus the bulk momentum-space Hamiltonian of the system becomes

$$h(k) = \begin{pmatrix} 0 & w + ve^{-ik} \\ w + ve^{ik} & 0 \end{pmatrix}, \quad \text{(C8)}$$

and we have $\boldsymbol{h}(k) = d_x(k) + id_y(k) = w + ve^{ik}$ where $d_x(k) = w + v\cos k$, $d_y(k) = v\sin k$.

Fig. 9(e) shows that the winding number of this SSH model with an odd number of qubits is always 1 whether $v < w$ or $v > w$. The wavefunctions of two edge states are presented in Fig. 9(f).

Appendix D: 3-qubit state transfer

Let us now further illustrate our proposal for 3-qubit entangled state transfer, i.e., $\mathcal{N}=3$ as an example. In this case, the qubit chain contains $\mathcal{L}=4M-1$ qubits and the corresponding Hamiltonian is given by Eq. (27) with $\mathcal{N}=3$ as

$$H=\sum_{m=1}^{M-1}\left(v\sigma_{A_{1,m}}^{+}\sigma_{B_m}^{-}+w\sigma_{A_{1,m+1}}^{+}\sigma_{B_m}^{-}+\text{H.c.}\right)+\sum_{m=1}^{M}\left(g\sigma_{A_{1,m}}^{+}\sigma_{A_{2,m}}^{-}+g\sigma_{A_{2,m}}^{+}\sigma_{A_{3,m}}^{-}+\text{H.c.}\right) \tag{D1}$$

The edge states are only localized in all A-type qubits (i.e., $A_{1,m}$-, $A_{2,m}$-, and $A_{3,m}$-type) and can be expanded as

$$|\Psi_{\text{edge}}\rangle=\sum_{m=1}^{M}\lambda^m\left(a\sigma_{A_{1,m}}^{+}+b\sigma_{A_{2,m}}^{+}+c\sigma_{A_{3,m}}^{+}\right)|G\rangle. \tag{D2}$$

Substituting this equation into eigen-energy function $H|\Psi_{\text{edge}}\rangle=E|\Psi_{\text{edge}}\rangle$, we have

$$\begin{aligned}&E\left(a\sigma_{A_{1,m}}^{+}+b\sigma_{A_{2,m}}^{+}+c\sigma_{A_{3,m}}^{+}\right)|G\rangle\\&=g\left(b\sigma_{A_{1,m}}^{+}+a\sigma_{A_{2,m}}^{+}+c\sigma_{A_{2,m}}^{+}+b\sigma_{A_{3,m}}^{+}\right)|G\rangle\\&+a\left(v\sigma_{B_m}^{+}+w\lambda\sigma_{B_m}^{+}\right)|G\rangle.\end{aligned} \tag{D3}$$

Here, for this special case of 3-qubit entangled state transfer, we have assumed that the coupling constant g_1 between $A_{1,m}$-qubit and $A_{2,m}$-qubit equals to that g_2 between $A_{2,m}$-qubit and $A_{3,m}$-qubit, i.e., $g_1=g_2=g$.

It is straightforward to obtain $\lambda=-v/w$, and the coefficients a, b, and c satisfy the following eigen-equation

$$\begin{pmatrix}0&g&0\\g&0&g\\0&g&0\end{pmatrix}\begin{pmatrix}a\\b\\c\end{pmatrix}=E\begin{pmatrix}a\\b\\c\end{pmatrix}. \tag{D4}$$

Solving Eq. (D4), we can obtain three eigenvalues $E_{\pm}=\pm\sqrt{2}g$ and $E_0=0$, corresponding to three eigenstates $\left(1/2,\pm\sqrt{2}/2,1/2\right)$ and $\left(1/\sqrt{2},0,-1/\sqrt{2}\right)$, respectively. These three eigenvalues are also eigenenergies of three edge states. Thus, three edge states are constructed by the eigenstates, i.e., $|\chi_{m,\pm}\rangle=\left(|\mathcal{A}_{1,m}\rangle\pm\sqrt{2}|\mathcal{A}_{2,m}\rangle+|\mathcal{A}_{3,m}\rangle\right)/2$ and $|\chi_{m,0}\rangle=\left(|\mathcal{A}_{1,m}\rangle-|\mathcal{A}_{3,m}\rangle\right)/\sqrt{2}$ associated with the mth unit cell. As shown in Eq. (D2), then these edge states can be given as

$$\begin{aligned}|\Psi_{\pm}\rangle=&\sum_{m=1}^{M}\lambda^m\left(\frac{\sigma_{A_{1,m}}^{+}\pm\sqrt{2}\sigma_{A_{2,m}}^{+}+\sigma_{A_{3,m}}^{+}}{2}\right)|G\rangle\\|\Psi_0\rangle=&\sum_{m=1}^{M}\lambda^m\left(\frac{\sigma_{A_{1,m}}^{+}-\sigma_{A_{3,m}}^{+}}{\sqrt{2}}\right)|G\rangle.\end{aligned} \tag{D5}$$

When $|\lambda|\ll 1$, i.e., $v\ll w$, the edge states are mainly localized at the left end of the chain, and when $|\lambda|\gg 1$, i.e., $v\gg w$, the edge states are mainly localized at the right end of the chain. In particular, when $v=0$, these edge states are written as $|L_{\pm}\rangle=|\chi_{1,\pm}\rangle|gg\cdots g\rangle$ and $|L_0\rangle=|\chi_{1,0}\rangle|gg\cdots g\rangle$, supported by the transport qubits on the left end of the chain. However, when $w=0$, the edge states are $|R_{\pm}\rangle=|gg\cdots g\rangle|\chi_{M,\pm}\rangle$ and $|R_0\rangle=|gg\cdots g\rangle|\chi_{M,0}\rangle$, supported by the transport qubits on the right end of the chain.

As discussed above, we can change the coupling constants slowly as $v=J\left[1-\cos\left(\omega t\right)\right]$ and $w=J\left[1+\cos\left(\omega t\right)\right]$, then the edge states of the system will adiabatically evolve from the left end to the right end of the chain. As shown in Fig. 5(a), using a qubit chain with $M=6$ unit cells (i.e., 23 qubits) as an example, we plot the variations of the instantaneous eigeneneries from $t=0$ to π/ω. We find that there are four bands of bulk states, separated by three topological edge states. The bulk bands outside of the edge states are not degenerate, however, each bulk band inside the gap of the edge states has five-fold degenerate. This has been further illustrated in Fig. 5(b) by arranging 23 eigenenstates by the corresponding eigenenergies (from the lowest to the highest), when the time t is taken as $t=\pi/6\omega$. Figure 5(a) also shows if the system is prepared to one of the left edge states ($|L_{\pm}\rangle$ and $|L_0\rangle$) at $t=0$, then the state will evolve to the corresponding right edge state ($|R_{\pm}\rangle$ or $|R_0\rangle$) when $t_f=\pi/\omega$.

More generally, if the initial state is prepared to an arbitrary 3-qubit entangled state at the left end of the chain as

$$|\Psi_{\text{in}}\rangle=\left(\alpha\sigma_{A_{1,1}}^{+}+\beta\sigma_{A_{2,1}}^{+}+\gamma\sigma_{A_{3,1}}^{+}\right)|G\rangle, \tag{D6}$$

which can be rewritten as

$$|\Psi_{\text{in}}\rangle=\frac{\alpha+\sqrt{2}\beta+\gamma}{2}|L_{+}\rangle+\frac{\alpha-\sqrt{2}\beta+\gamma}{2}|L_{-}\rangle+\frac{\alpha-\gamma}{\sqrt{2}}|L_0\rangle, \tag{D7}$$

by using the left edge states, then the state will adiabatically evolve to

$$\begin{aligned}|\Psi\left(t\right)\rangle=&\frac{\alpha+\sqrt{2}\beta+\gamma}{2}|\Psi_{+}\left(t\right)\rangle e^{-i\int_0^t E_{+}dt'}\\&+\frac{\alpha-\sqrt{2}\beta+\gamma}{2}|\Psi_{-}\left(t\right)\rangle e^{-i\int_0^t E_{-}dt'}\\&+\frac{\alpha-\gamma}{\sqrt{2}}|\Psi_0\left(t\right)\rangle e^{-i\int_0^t E_0dt'},\end{aligned} \tag{D8}$$

at the moment t. As we learn from the case of the two-qubit state transfer, $E_{\pm}=\pm\sqrt{2}g$ and $E_0=0$ here are still constant during the adiabatic protocol, thus the final

state at $t_f = \pi/\omega$ is

$$|\Psi_f\rangle = \frac{\alpha+\sqrt{2}\beta+\gamma}{2}|R_+\rangle e^{-i2\pi\frac{g}{\sqrt{2}w}} + \frac{\alpha-\sqrt{2}\beta+\gamma}{2}|R_-\rangle e^{i2\pi\frac{g}{\sqrt{2}w}} + \frac{\alpha-\gamma}{\sqrt{2}}|R_0\rangle. \quad \text{(D9)}$$

Again, let us consider the evolution time to be exact integral multiples of the dynamical period $T = 2\pi/\sqrt{2}g$, i.e., $t_f/T = g/\sqrt{2}\omega = n$ ($n \gg 1$), then the final state becomes

$$|\Psi_F\rangle = \left(\alpha\sigma^+_{A_{1,M}} + \beta\sigma^+_{A_{2,M}} + \gamma\sigma^+_{A_{3,M}}\right)|G\rangle. \quad \text{(D10)}$$

Clearly then, as time t changes from 0 to π/ω, arbitrary 3-qubit entangled state can be transported from the left end to the right end of the chain.

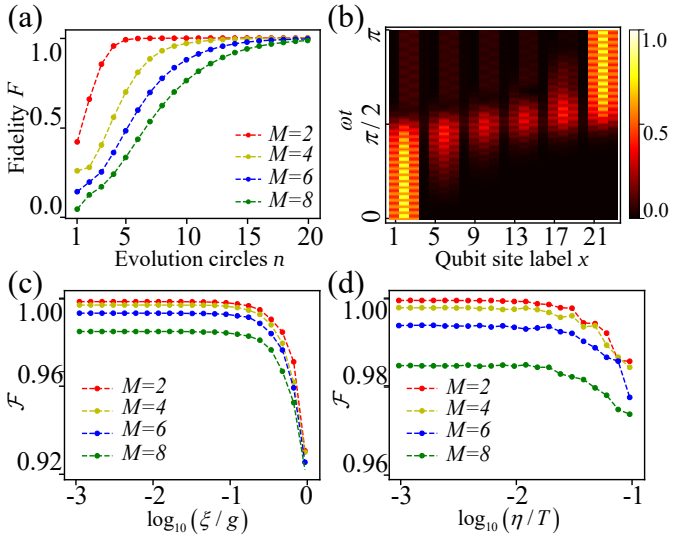

Figure 10. 3-qubit state transfer with extended SSH4 chain. The parameters are taken as $J = 5g$ and $g/2\pi = 10$MHz. (a) Target-state occupation probabilities $F(nT) = |\langle\Psi_F|\Psi(nT)\rangle|$ as a function of the number of evolution cycles n. Each point represents a complete adiabatic evolution from $t = 0$ to $t = \pi/\omega$. Various colors from red to green represent different lengths of the chain, where $M = 2, 4, 6, 8$. (b) Time evolution of the whole qubit-chain state with initial state prepared to a three-qubit W state $(|\mathcal{A}_{1,1}\rangle + |\mathcal{A}_{2,1}\rangle + |\mathcal{A}_{3,1}\rangle)/\sqrt{3}$ when the total evolution time is 20 evolution cycles n. The color from dark-red to bright-yellow represents the population distribution of the state on each qubit site. (c) The average fidelities of 3-qubit W-state transfer with different coupling disorder strength. $M = 2, 4, 6, 8$ for each curve, separately. (d) The average fidelities of 3-qubit W-state transfer with different execution time disorder.

Same as the case of 2-qubit state transfer, we choose different numbers of evolution cycles to examine the adiabaticity. In Fig. 10(a), target-state occupation probabilities $F(t) = |\langle\Psi_F|\Psi(t)\rangle|$ are plotted as a function of the number of evolution cycles when a W-state is transferred from the left edge to the right one for different lengths of the chain. We find that the evolution cycles to achieve high fidelity increase with the length M of the chain when the qubit number in the unit cell is given. For example, Fig. 10(a) shows that 20 evolving cycles are required to achieve fidelity one when $M = 8$, however 5 evolving cycles are enough to achieve fidelity one when $M = 2$. For a specific case shown in Fig. 10(b), the W state is shown to be transferring from the left to the right with a rapid oscillation within the execution time (20 evolution cycles). In Fig. 10(c), we have also evaluated the average fidelities of the 3-qubit W-state transfer with different disorder strengths ξ for the coupling strengths. There is also a plateau at $\xi \in [10^{-3}g, 10^{-1}g]$ for each qubit chain. However, different from the two-qubit transfer, these plateaus are pinned at different values of fidelity with the increase of the qubit number. We find that the average fidelity for all the qubit chains considered here is far beyond 96% so long as the disorder strength is $\xi < 0.1g$. Meanwhile, the effect of the disorder of the time evolution is presented in Fig. 10(d). The average fidelity $\mathcal{F}$ is also good enough for state transfer as the disorder strength η is less than $0.01T$. Figs. 10(c) and (d) clearly show that our proposal is also promising for transferring 3-qubit state along a long qubit chain.

Appendix E: Energy spectrum detecting with Input-output theory

To estimate the dynamical period in our QST protocol, one can measure the eigen-energy spectrum of edge states with input-output theory for our extended SSH chain. Specifically, for the 2-qubit state transfer as discussed above, the energy difference between the two edge states of the chain is $2g$. Meanwhile, for the 3-qubit state transfer protocol, the energy difference between the three edge states of the chain is $\sqrt{2}g$. To measure the energy spectrum of the extended SSH chain, we assume that a weak probe field is applied to the qubit chian via a transmission line. Thus, the energy spectrum can be detected by the transmission or reflection of the probe light. This setup is schematically shown in Fig. 11(a).

For the convenience of derivation, we here consider a generic qubit chain with arbitrary qubit-qubit couplings. The Hamiltonian of this qubit chain can be written as

$$H_{\text{qubits}} = \sum_{x=1}^{\mathcal{L}} \omega_x \sigma_x^+ \sigma_x^- + \sum_{x,y}^{x\neq y} \left(\Omega_{x,y}\sigma_x^+\sigma_y^- + \text{H.c.}\right) \quad \text{(E1)}$$

Here ω_x is the frequency of the xth qubit, and $\Omega_{x,y}$ ($x, y \in \{1, \cdots, \mathcal{L}\}$) is the coupling strength between xth and yth qubits. When coupled with the transmission line, the

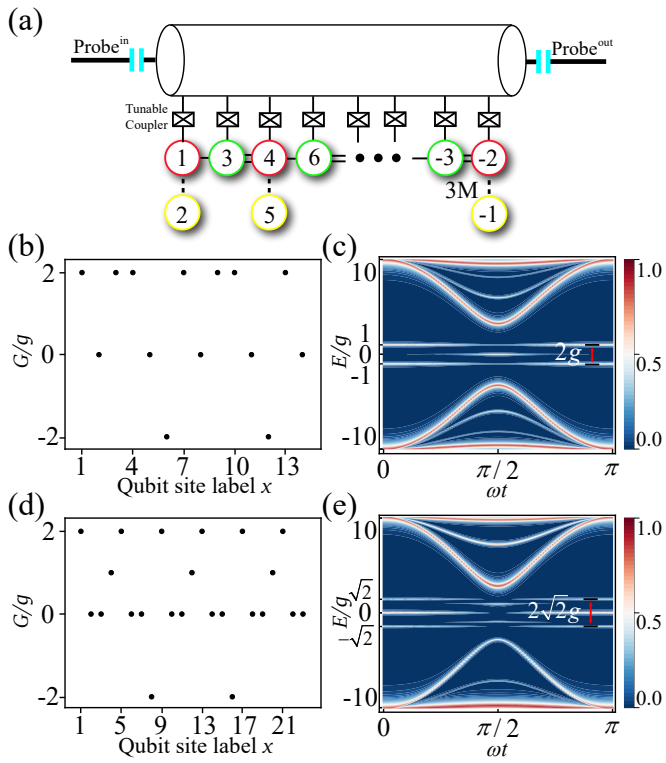

Figure 11. (a) Schematic diagram for the SSH qubit array detected by a microwave transmission line. The transmission line here is coupled to the qubit chain with a set of josephson couplers, and the coupling strength between each qubit and the waveguide is tunable by the coupler. The transmission line can be seen as a long waveguide with infinite microwave modes. The frequency of input probe light is tunable and we can get the energy spectrum of the qubit chain by detecting the transmission of the probe light. (b) Inhomogeneous couplings between the waveguide and qubits for the extended SSH chain in Fig. 2(a). (c) Energy spectrum of the qubit chain for 2-qubit state transfer with waveguide-qubit couplings in (b). (d) Inhomogeneous couplings between the waveguide and qubits for the extended SSH chain in Fig. 10(a). (e) Energy spectrum of the qubit chain for 3-qubit state transfer with waveguide-qubit couplings in (d).

Hamiltonian of whole system will become

$$H = H_{\text{qubits}} + \omega_c a^\dagger a + \sum_{x=1}^{\mathcal{L}} G_x \left(\sigma_x^+ a + \sigma_x^- a^\dagger\right) + \varepsilon \left(a e^{i\omega_p t} + a^\dagger e^{-i\omega_p t}\right), \tag{E2}$$

where ω_c is the frequency of waveguide mode, G_x is the coupling strength between waveguide and xth qubit, and ε is the driving strength of the probe light. After rotating-wave approximation by applying a unitary operator $U = \exp\left(\omega_p a^\dagger a t + \sum_{x=1}^{\mathcal{L}} \omega_p \sigma_x^+ \sigma_x^- t\right)$, we get the effective Hamiltonian as

$$H_{eff} = \sum_{x=1}^{\mathcal{L}} \triangle_x \sigma_x^+ \sigma_x^- + \sum_{x,y}^{x\neq y} \left(\Omega_{x,y} \sigma_x^+ \sigma_y^- + \text{H.c.}\right) + \triangle_c a^\dagger a + \sum_{x=1}^{\mathcal{L}} G_x \left(\sigma_x^+ a + \sigma_x^- a^\dagger\right) + \varepsilon \left(a + a^\dagger\right), \tag{E3}$$

where $\triangle_x = \omega_x - \omega_p$ and $\triangle_c = \omega_c - \omega_p$ are the detuning frequency for qubits and waveguide, respectively. The waveguide naturally has infinite modes and only the mode resonating with the probe light has contribution to the Hamiltonian, i.e., $\omega_c = \omega_p$. Thus we can have $\triangle_c = 0$. We here consider the low-excitation limit, so the evolutions of operators' average value can be derived as

$$\dot{\langle a \rangle} = -\left(\kappa + i\triangle_c\right)\langle a \rangle - i \sum_{x=1}^{\mathcal{L}} G_x \left\langle \sigma_x^- \right\rangle + \varepsilon \tag{E4}$$

$$\dot{\left\langle \sigma_x^- \right\rangle} = -i\triangle_x \left\langle \sigma_x^- \right\rangle - iG_x \langle a \rangle - i \sum_{y=1}^{\mathcal{L}} \Omega_{x,y} \left\langle \sigma_y^- \right\rangle - \Gamma_x \left\langle \sigma_x^- \right\rangle, \tag{E5}$$

where κ is decay rate for the waveguide and Γ_x is the decay of xth qubit. The evolution equations above can be written into matrix form as

$$\dot{\langle a \rangle} = -\left(\kappa + i\triangle_c\right)\langle a \rangle - i\boldsymbol{G}^T \boldsymbol{\sigma} + \varepsilon \tag{E6}$$

$$\dot{\langle \boldsymbol{\sigma} \rangle} = -i\left(\triangle + \boldsymbol{\Omega} - i\boldsymbol{\Gamma}\right)\langle \boldsymbol{\sigma} \rangle - i\boldsymbol{G}\langle a \rangle, \tag{E7}$$

where $\boldsymbol{\sigma} = \left(\left\langle \sigma_1^- \right\rangle, \left\langle \sigma_2^- \right\rangle, \cdots \left\langle \sigma_{\mathcal{L}}^- \right\rangle\right)^T$, $\triangle = \text{Diag}\left(\triangle_1, \triangle_2, \cdots, \triangle_{\mathcal{L}}\right)$, $\boldsymbol{\Gamma} = \text{Diag}\left(\Gamma_1, \Gamma_2, \cdots, \Gamma_{\mathcal{L}}\right)$, $\boldsymbol{G} = \left(G_1, G_2, \cdots, G_{\mathcal{L}}\right)^T$ and $\boldsymbol{\Omega}$ has the matrix form of the coupling terms in H_{qubits}, i.e., $\boldsymbol{\Omega}_{x,y} = \Omega_{x,y}$. Here, notice that for our measurement setup as shown in Fig. 11(a), the transmission line only couples to the top half of the chain. This feature can be reflected by the coupling coefficient G_x as shown in Fig. 11(b) and (d).

When the system is stable, i.e., $\dot{\langle a \rangle} = \dot{\boldsymbol{\sigma}} = 0$, we can get the steady solution of the equations as

$$\boldsymbol{\sigma} = -i\boldsymbol{M}^{-1}\boldsymbol{G}\langle a \rangle \tag{E8}$$

$$\langle a \rangle = \frac{\varepsilon}{\kappa + i\triangle_c + \boldsymbol{G}^T\boldsymbol{M}^{-1}\boldsymbol{G}} \tag{E9}$$

where $\boldsymbol{M} = i\triangle + i\boldsymbol{\Omega} + \boldsymbol{\Gamma}$. From the input-output theory, the transmission of the probe field is

$$t_p = 1 - \frac{\kappa}{\varepsilon}\langle a \rangle = 1 - \frac{\kappa}{\kappa + i\triangle_c + \boldsymbol{G}^T\boldsymbol{M}^{-1}\boldsymbol{G}}, \tag{E10}$$

and therefore the reflection of the probe field is

$$r_p = \frac{\kappa}{\kappa + i\triangle_c + \boldsymbol{G}^T \boldsymbol{M}^{-1} \boldsymbol{G}}. \tag{E11}$$

For the 2-qubit state transfer protocol with 14 qubits chain in Fig. 2(a), all the qubits are resonating with each other, i.e., $\omega_x = \omega_q$ for $x = 1, 2, ..., \mathcal{L}$. Therefore we have $\triangle = \mathrm{Diag}\,(\triangle_q, \triangle_q, \triangle_q, \cdots, \triangle_q)$ and $\triangle_q = \omega_q - \omega_p$. $\boldsymbol{\Omega}$ is the matrix form of the Hamiltonian shown in Eq. (2). The decay of the waveguide is $\kappa = 2.5g$ and all the qubits have the same decay rate as $\gamma = 0.01g$. The coupling strengths $\boldsymbol{G}$ between qubits and waveguide are shown in Fig. 11(b). From Eq. (E11) we can get the reflection spectrum of the qubit chain for different probe light as shown in Fig. 11(c), where the vertical coordinates represent the detuning frequency $\triangle_q$ and also the eigen-energy of the system. Two edge states are clearly shown in the figure and we can get the energy shift as $2g$. Another case we show here is the 23 qubits chain for 3-qubit state transfer, and we can also get the energy shift as $2\sqrt{2}g$ in Fig. 11(e).

[1] A. Steane, Quantum computing, Rep. Prog. Phys. **61**, 117 (1998).
[2] J. Preskill, Quantum Computing in the NISQ era and beyond, Quantum **2**, 79 (2018).
[3] C. H. Bennett and D. P. DiVincenzo, Quantum information and computation, Nature **404**, 247 (2000).
[4] D. S. Weiss and M. Saffman, Quantum computing with neutral atoms, Phys. Today **70** (2017).
[5] A. Negretti, P. Treutlein, and T. Calarco, Quantum computing implementations with neutral particles, Quantum Inf. Process. **10**, 721 (2011).
[6] H.-J. Briegel, T. Calarco, D. Jaksch, J. I. Cirac, and P. Zoller, Quantum computing with neutral atoms, J. Mod. Opt. **47**, 415 (2000).
[7] J. J. García-Ripoll, P. Zoller, and J. I. Cirac, Quantum information processing with cold atoms and trapped ions, J. Phys. B: At. Mol. Opt. Phys. **38**, S567 (2005).
[8] H. Häffner, C. F. Roos, and R. Blatt, Quantum computing with trapped ions, Phys. Rep. **469**, 155 (2008).
[9] J. Benhelm, G. Kirchmair, C. F. Roos, and R. Blatt, Towards fault-tolerant quantum computing with trapped ions, Nat. Phys. **4**, 463 (2008).
[10] C. D. Bruzewicz, J. Chiaverini, R. McConnell, and J. M. Sage, Trapped-ion quantum computing: Progress and challenges, Appl. Phys. Rev. **6**, 021314 (2019).
[11] J. I. Cirac and P. Zoller, A scalable quantum computer with ions in an array of microtraps, Nature **404**, 579 (2000).
[12] B. P. Lanyon, P. Jurcevic, M. Zwerger, C. Hempel, E. A. Martinez, W. Dür, H. J. Briegel, R. Blatt, and C. F. Roos, Measurement-based quantum computation with trapped ions, Phys. Rev. Lett. **111**, 210501 (2013).
[13] J. J. García-Ripoll, P. Zoller, and J. I. Cirac, Speed optimized two-qubit gates with laser coherent control techniques for ion trap quantum computing, Phys. Rev. Lett. **91**, 157901 (2003).
[14] J. Pachos and H. Walther, Quantum computation with trapped ions in an optical cavity, Phys. Rev. Lett. **89**, 187903 (2002).
[15] M. Feng, Quantum computing with trapped ions in an optical cavity via Raman transition, Phys. Rev. A **66**, 054303 (2002).
[16] E. Jeffrey, D. Sank, J. Y. Mutus, T. C. White, J. Kelly, R. Barends, Y. Chen, Z. Chen, B. Chiaro, A. Dunsworth, A. Megrant, P. J. J. O'Malley, C. Neill, P. Roushan, A. Vainsencher, J. Wenner, A. N. Cleland, and J. M. Martinis, Fast Accurate State Measurement with Superconducting Qubits, Phys. Rev. Lett. **112**, 190504 (2014).
[17] J. M. Gambetta, J. M. Chow, and M. Steffen, Building logical qubits in a superconducting quantum computing system, Npj Quantum Inf. **3**, 1 (2017).
[18] T. Brecht, W. Pfaff, C. Wang, Y. Chu, L. Frunzio, M. H. Devoret, and R. J. Schoelkopf, Multilayer microwave integrated quantum circuits for scalable quantum computing, Npj Quantum Inf. **2**, 1 (2016).
[19] M. H. Devoret, A. Wallraff, and J. M. Martinis, Superconducting qubits: A short review, arXiv preprint cond-mat/0411174 (2004).
[20] J. You and F. Nori, Superconducting Circuits and Quantum Information, Physics Today **58**, 42 (2005).
[21] Z. Yan, Y.-R. Zhang, M. Gong, Y. Wu, Y. Zheng, S. Li, C. Wang, F. Liang, J. Lin, Y. Xu, C. Guo, L. Sun, C.-Z. Peng, K. Xia, H. Deng, H. Rong, J. Q. You, F. Nori, H. Fan, X. Zhu, and P. Jian-Wei, Strongly correlated quantum walks with a 12-qubit superconducting processor, Science **364**, 753 (2019).
[22] C. Song, K. Xu, W. Liu, C.-p. Yang, S.-B. Zheng, H. Deng, Q. Xie, K. Huang, Q. Guo, L. Zhang, P. Zhang, D. Xu, D. Zheng, X. Zhu, H. Wang, Y.-A. Chen, C.-Y. Lu, S. Han, and J.-W. Pan, 10-Qubit Entanglement and Parallel Logic Operations with a Superconducting Circuit, Phys. Rev. Lett. **119**, 180511 (2017).
[23] C. Neill, P. Roushan, K. Kechedzhi, S. Boixo, S. V. Isakov, V. Smelyanskiy, A. Megrant, B. Chiaro, A. Dunsworth, K. Arya, R. Barends, B. Burkett, Y. Chen, Z. Chen, A. Fowler, B. Foxen, M. Giustina, R. Graff, E. Jeffrey, T. Huang, J. Kelly, P. Klimov, E. Lucero, J. Mutus, M. Neeley, C. Quintana, D. Sank, A. Vainsencher, J. Wenner, T. C. White, H. Neven, and J. M. Martinis, A blueprint for demonstrating quantum supremacy with superconducting qubits, Science **360**, 195 (2018).
[24] H.-L. Huang, D. Wu, D. Fan, and X. Zhu, Superconducting quantum computing: a review, Sci. China Inf. Sci. **63**, 1 (2020).
[25] P. Krantz, M. Kjaergaard, F. Yan, T. P. Orlando, S. Gustavsson, and W. D. Oliver, A quantum engineer's guide to superconducting qubits, Appl. Phys. Rev. **6**, 021318 (2019).
[26] J. Q. You and F. Nori, Quantum information processing with superconducting qubits in a microwave field, Phys. Rev. B **68**, 064509 (2003).
[27] K. Osborn, J. Strong, A. J. Sirois, and R. W. Simmonds,

Frequency-tunable Josephson junction resonator for quantum computing, IEEE Trans. Appl. Supercond. **17**, 166 (2007).
[28] M. Pechal, P. Arrangoiz-Arriola, and A. H. Safavi-Naeini, Superconducting circuit quantum computing with nanomechanical resonators as storage, Quantum Sci. Technol. **4**, 015006 (2018).
[29] D. Bouwmeester and A. Zeilinger, *The physics of quantum information* (Springer, Berlin, Heidelberg, 2000).
[30] F. Zhu, W. Zhang, Y. Sheng, and Y. Huang, Experimental long-distance quantum secure direct communication, Sci. Bull. **62**, 1519 (2017).
[31] X. Liu, X. Yao, H. Wang, H. Li, Z. Wang, L. You, Y. Huang, and W. Zhang, Energy-time entanglement-based dispersive optics quantum key distribution over optical fibers of 20 km, Appl. Phys. Lett. **114**, 141104 (2019).
[32] M. Huo, J. Qin, J. Cheng, Z. Yan, Z. Qin, X. Su, X. Jia, C. Xie, and K. Peng, Deterministic quantum teleportation through fiber channels, Sci. Adv. **4**, eaas9401 (2018).
[33] Y.-A. Chen, Q. Zhang, T.-Y. Chen, W.-Q. Cai, S.-K. Liao, J. Zhang, K. Chen, J. Yin, J.-G. Ren, Z. Chen, S.-L. Han, Q. Yu, K. Liang, F. Zhou, X. Yuan, M.-S. Zhao, T.-Y. Wang, X. Jiang, L. Zhang, W.-Y. Liu, Y. Li, Q. Shen, Y. Cao, C.-Y. Lu, R. Shu, J.-Y. Wang, L. Li, N.-L. Liu, F. Xu, X.-B. Wang, C.-Z. Peng, and J.-W. Pan, An integrated space-to-ground quantum communication network over 4,600 kilometres, Nature **589**, 214 (2021).
[34] S.-K. Liao, W.-Q. Cai, J. Handsteiner, B. Liu, J. Yin, L. Zhang, D. Rauch, M. Fink, J.-G. Ren, W.-Y. Liu, Y. Li, Q. Shen, Y. Cao, F.-Z. Li, J.-F. Wang, Y.-M. Huang, L. Deng, T. Xi, L. Ma, T. Hu, L. Li, N.-L. Liu, F. Koidl, P. Wang, Y.-A. Chen, X.-B. Wang, M. Steindorfer, G. Kirchner, C.-Y. Lu, R. Shu, R. Ursin, T. Scheidl, C.-Z. Peng, J.-Y. Wang, A. Zeilinger, and J.-W. Pan, Satellite-Relayed Intercontinental Quantum Network, Phys. Rev. Lett. **120**, 030501 (2018).
[35] S. Bose, Quantum communication through an unmodulated spin chain, Phys. Rev. Lett. **91**, 207901 (2003).
[36] M. Christandl, N. Datta, A. Ekert, and A. J. Landahl, Perfect state transfer in quantum spin networks, Phys. Rev. Lett. **92**, 187902 (2004).
[37] V. Balachandran and J. Gong, Adiabatic quantum transport in a spin chain with a moving potential, Phys. Rev. A **77**, 012303 (2008).
[38] Z. Song and C. Sun, Quantum information storage and state transfer based on spin systems, Low Temp. Phys. **31**, 686 (2005).
[39] M.-H. Yung, Quantum speed limit for perfect state transfer in one dimension, Phys. Rev. A **74**, 030303(R) (2006).
[40] M.-H. Yung and S. Bose, Perfect state transfer, effective gates, and entanglement generation in engineered bosonic and fermionic networks, Phys. Rev. A **71**, 032310 (2005).
[41] L.-A. Wu, A. Miranowicz, X. B. Wang, Y.-X. Liu, and F. Nori, Perfect function transfer and interference effects in interacting boson lattices, Phys. Rev. A **80**, 012332 (2009).
[42] L.-A. Wu, Y.-X. Liu, and F. Nori, Universal existence of exact quantum state transmissions in interacting media, Phys. Rev. A **80**, 042315 (2009).
[43] A. Bienfait, K. J. Satzinger, Y. P. Zhong, H. S. Chang, M. H. Chou, C. R. Conner, É. Dumur, J. Grebel, G. A. Peairs, R. G. Povey, and A. N. Cleland, Phonon-mediated quantum state transfer and remote qubit entanglement, Science **364**, 368 (2019).
[44] E. A. Sete and H. Eleuch, High-efficiency quantum state transfer and quantum memory using a mechanical oscillator, Phys. Rev. A **91**, 032309 (2015).
[45] B. Vermersch, P.-O. Guimond, H. Pichler, and P. Zoller, Quantum state transfer via noisy photonic and phononic waveguides, Phys. Rev. Lett. **118**, 133601 (2017).
[46] Y. He, Y.-M. He, Y.-J. Wei, X. Jiang, K. Chen, C.-Y. Lu, J.-W. Pan, C. Schneider, M. Kamp, and S. Höfling, Quantum state transfer from a single photon to a distant quantum-dot electron spin, Phys. Rev. Lett. **119**, 060501 (2017).
[47] N. Maring, P. Farrera, K. Kutluer, M. Mazzera, G. Heinze, and H. de Riedmatten, Photonic quantum state transfer between a cold atomic gas and a crystal, Nature **551**, 485 (2017).
[48] T. Northup and R. Blatt, Quantum information transfer using photons, Nat. Photonics **8**, 356 (2014).
[49] J. I. Cirac, P. Zoller, H. J. Kimble, and H. Mabuchi, Quantum state transfer and entanglement distribution among distant nodes in a quantum network, Phys. Rev. Lett. **78**, 3221 (1997).
[50] T. Shi, Y. Li, Z. Song, and C.-P. Sun, Quantum-state transfer via the ferromagnetic chain in a spatially modulated field, Phys. Rev. A **71**, 032309 (2005).
[51] A. Zwick, G. A. Álvarez, J. Stolze, and O. Osenda, Robustness of spin-coupling distributions for perfect quantum state transfer, Phys. Rev. A **84**, 022311 (2011).
[52] Y. P. Kandel, H. Qiao, S. Fallahi, G. C. Gardner, M. J. Manfra, and J. M. Nichol, Adiabatic quantum state transfer in a semiconductor quantum-dot spin chain, Nat. Commun. **12**, 1 (2021).
[53] N. Y. Yao, L. Jiang, A. V. Gorshkov, Z.-X. Gong, A. Zhai, L.-M. Duan, and M. D. Lukin, Robust Quantum State Transfer in Random Unpolarized Spin Chains, Phys. Rev. Lett. **106**, 040505 (2011).
[54] S. Bose, Quantum communication through spin chain dynamics: an introductory overview, Contemp. Phys. **48**, 13 (2007).
[55] F. Mei, G. Chen, L. Tian, S.-L. Zhu, and S. Jia, Robust quantum state transfer via topological edge states in superconducting qubit chains, Phys. Rev. A **98**, 012331 (2018).
[56] S. Longhi, Topological pumping of edge states via adiabatic passage, Phys. Rev. B **99**, 155150 (2019).
[57] F. M. D'Angelis, F. A. Pinheiro, D. Guéry-Odelin, S. Longhi, and F. Impens, Fast and robust quantum state transfer in a topological Su-Schrieffer-Heeger chain with next-to-nearest-neighbor interactions, Phys. Rev. Res. **2**, 033475 (2020).
[58] R. Wang, X. Z. Zhang, and Z. Song, Dynamical topological invariant for the non-Hermitian Rice-Mele model, Phys. Rev. A **98**, 042120 (2018).
[59] J. Zhang, G. L. Long, W. Zhang, Z. Deng, W. Liu, and Z. Lu, Simulation of Heisenberg XY interactions and realization of a perfect state transfer in spin chains using liquid nuclear magnetic resonance, Phys. Rev. A **72**, 012331 (2005).
[60] D. Petrosyan, G. M. Nikolopoulos, and P. Lambropoulos, State transfer in static and dynamic spin chains with

disorder, Phys. Rev. A **81**, 042307 (2010).
[61] G. Gualdi, V. Kostak, I. Marzoli, and P. Tombesi, Perfect state transfer in long-range interacting spin chains, Phys. Rev. A **78**, 022325 (2008).
[62] A. Kay, Perfect, Effecient, State Transfer and its Application as a Constructive Tool, Int. J. Quantum Inf. **08**, 641 (2010).
[63] R. Ronke, M. P. Estarellas, I. D'Amico, T. P. Spiller, and T. Miyadera, Anderson localisation in spin chains for perfect state transfer, Eur. Phys. J. D **70**, 1 (2016).
[64] Z.-M. Wang, M. S. Sarandy, and L.-A. Wu, Almost exact state transfer in a spin chain via pulse control, Phys. Rev. A **102**, 022601 (2020).
[65] A. O. Lyakhov and C. Bruder, Use of dynamical coupling for improved quantum state transfer, Phys. Rev. B **74**, 235303 (2006).
[66] A. Zwick, G. A. Álvarez, G. Bensky, and G. Kurizki, Optimized dynamical control of state transfer through noisy spin chains, New J. Phys. **16**, 065021 (2014).
[67] S. C. Benjamin, Quantum computing without local control of qubit-qubit interactions, Phys. Rev. Lett. **88**, 017904 (2001).
[68] S. C. Benjamin and S. Bose, Quantum computing with an always-on Heisenberg interaction, Phys. Rev. Lett. **90**, 247901 (2003).
[69] S. Tan, R. W. Bomantara, and J. Gong, High-fidelity and long-distance entangled-state transfer with Floquet topological edge modes, Phys. Rev. A **102**, 022608 (2020).
[70] M. Demirplak and S. A. Rice, Adiabatic population transfer with control fields, J. Phys. Chem. A **107**, 9937 (2003).
[71] J. Gong and S. A. Rice, Complete quantum control of the population transfer branching ratio between two degenerate target states, J. Chem. Phys. **121**, 1364 (2004).
[72] J. Gong and S. A. Rice, Adiabatic population transfer in a liquid: Taking advantage of a decaying target state, J. Chem. Phys. **120**, 3777 (2004).
[73] K. Eckert, O. Romero-Isart, and A. Sanpera, Efficient quantum state transfer in spin chains via adiabatic passage, New J. Phys. **9**, 155 (2007).
[74] D. Y. H. Ho and J. Gong, Quantized adiabatic transport in momentum space, Phys. Rev. Lett. **109**, 010601 (2012).
[75] L. Tian, Adiabatic state conversion and pulse transmission in optomechanical systems, Phys. Rev. Lett. **108**, 153604 (2012).
[76] R. R. Agundez, C. D. Hill, L. C. L. Hollenberg, S. Rogge, and M. Blaauboer, Superadiabatic quantum state transfer in spin chains, Phys. Rev. A **95**, 012317 (2017).
[77] M. Sandberg, E. Knill, E. Kapit, M. R. Vissers, and D. P. Pappas, Efficient quantum state transfer in an engineered chain of quantum bits, Quantum Inf. Process. **15**, 1213 (2016).
[78] A. Messiah, *Quantum mechanics: volume II* (North-Holland, Amsterdam, 1964).
[79] M. V. Berry, Quantal phase factors accompanying adiabatic changes, Proc. Math. Phys. Eng. Sci. **392**, 45 (1984).
[80] M. Z. Hasan and C. L. Kane, Colloquium: topological insulators, Rev. Mod. Phys. **82**, 3045 (2010).
[81] X.-L. Qi and S.-C. Zhang, Topological insulators and superconductors, Rev. Mod. Phys. **83**, 1057 (2011).
[82] J. K. Asbóth, L. Oroszlány, and A. Pályi, A short course on topological insulators, Lect. Notes Phys. **919**, 997 (2016).
[83] H. Luo, *Advanced topological insulators* (Wiley Online Library, 2019).
[84] C. Nayak, S. H. Simon, A. Stern, M. Freedman, and S. DasSarma, Non-Abelian anyons and topological quantum computation, Rev. Mod. Phys. **80**, 1083 (2008).
[85] M. Freedman, A. Kitaev, M. Larsen, and Z. Wang, Topological quantum computation, Bull. Amer. Math. Soc. **40**, 31 (2003).
[86] A. Stern and N. H. Lindner, Topological quantum computation-from basic concepts to first experiments, Science **339**, 1179 (2013).
[87] R. W. Bomantara and J. Gong, Simulation of non-Abelian braiding in Majorana time crystals, Phys. Rev. Lett. **120**, 230405 (2018).
[88] R. W. Bomantara and J. Gong, Quantum computation via Floquet topological edge modes, Phys. Rev. B **98**, 165421 (2018).
[89] R. W. Bomantara and J. Gong, Measurement-only quantum computation with Floquet Majorana corner modes, Phys. Rev. B **101**, 085401 (2020).
[90] W. P. Su, J. R. Schrieffer, and A. J. Heeger, Solitons in polyacetylene, Phys. Rev. Lett. **42**, 1698 (1979).
[91] F. Mei, G. Chen, L. Tian, S.-L. Zhu, and S. Jia, Topology-dependent quantum dynamics and entanglement-dependent topological pumping in superconducting qubit chains, Phys. Rev. A **98**, 032323 (2018).
[92] N. Y. Yao, C. R. Laumann, A. V. Gorshkov, H. Weimer, L. Jiang, J. I. Cirac, P. Zoller, and M. D. Lukin, Topologically protected quantum state transfer in a chiral spin liquid, Nat. Commun. **4**, 1 (2013).
[93] N. Palaiodimopoulos, I. Brouzos, F. Diakonos, and G. Theocharis, Fast and robust quantum state transfer via a topological chain, Phys. Rev. A **103**, 052409 (2021).
[94] A. A. Houck, H. E. Türeci, and J. Koch, On-chip quantum simulation with superconducting circuits, Nat. Phys. **8**, 292 (2012).
[95] G. Paraoanu, Recent progress in quantum simulation using superconducting circuits, J. Low Temp. Phys. **175**, 633 (2014).
[96] P. Roushan, C. Neill, J. Tangpanitanon, V. M. Bastidas, A. Megrant, R. Barends, Y. Chen, Z. Chen, B. Chiaro, A. Dunsworth, A. Fowler, B. Foxen, M. Giustina, E. Jeffrey, J. Kelly, E. Lucero, J. Mutus, M. Neeley, C. Quintana, D. Sank, A. Vainsencher, J. Wenner, T. White, H. Neven, D. G. Angelakis, and J. Martinis, Spectroscopic signatures of localization with interacting photons in superconducting qubits, Science **358**, 1175 (2017).
[97] H. Paik, D. I. Schuster, L. S. Bishop, G. Kirchmair, G. Catelani, A. P. Sears, B. R. Johnson, M. J. Reagor, L. Frunzio, L. I. Glazman, S. M. Girvin, M. H. Devoret, and R. J. Schoelkopf, Observation of High Coherence in Josephson Junction Qubits Measured in a Three-Dimensional Circuit QED Architecture, Phys. Rev. Lett. **107**, 240501 (2011).
[98] S. Novikov, T. Sweeney, J. Robinson, S. Premaratne, B. Suri, F. Wellstood, and B. Palmer, Raman coherence in a circuit quantum electrodynamics lambda system, Nat. Phys. **12**, 75 (2016).
[99] Y. Chen, C. Neill, P. Roushan, N. Leung, M. Fang,

R. Barends, J. Kelly, B. Campbell, Z. Chen, B. Chiaro, A. Dunsworth, E. Jeffrey, A. Megrant, J. Y. Mutus, P. J. J. O'Malley, C. M. Quintana, D. Sank, A. Vainsencher, J. Wenner, T. C. White, M. R. Geller, A. N. Cleland, and J. M. Martinis, Qubit Architecture with High Coherence and Fast Tunable Coupling, Phys. Rev. Lett. **113**, 220502 (2014).

[100] M. R. Geller, E. Donate, Y. Chen, M. T. Fang, N. Leung, C. Neill, P. Roushan, and J. M. Martinis, Tunable coupler for superconducting Xmon qubits: Perturbative nonlinear model, Phys. Rev. A **92**, 012320 (2015).

[101] R. Barends, L. Lamata, J. Kelly, L. García-Álvarez, A. G. Fowler, A. Megrant, E. Jeffrey, T. C. White, D. Sank, J. Y. Mutus, B. Campbell, Y. Chen, Z. Chen, B. Chiaro, A. Dunsworth, I. C. Hoi, C. Neill, P. J. J. O'Malley, C. Quintana, P. Roushan, A. Vainsencher, J. Wenner, E. Solano, and J. M. Martinis, Digital quantum simulation of fermionic models with a superconducting circuit, Nat. Commun. **6**, 1 (2015).

[102] G. M. Reuther, D. Zueco, F. Deppe, E. Hoffmann, E. P. Menzel, T. Weißl, M. Mariantoni, S. Kohler, A. Marx, E. Solano, R. Gross, and P. Hänggi, Two-resonator circuit quantum electrodynamics: Dissipative theory, Phys. Rev. B **81**, 144510 (2010).

[103] A. Baust, E. Hoffmann, M. Haeberlein, M. J. Schwarz, P. Eder, J. Goetz, F. Wulschner, E. Xie, L. Zhong, F. Quijandría, B. Peropadre, D. Zueco, J.-J. García Ripoll, E. Solano, K. Fedorov, E. P. Menzel, F. Deppe, A. Marx, and R. Gross, Tunable and switchable coupling between two superconducting resonators, Phys. Rev. B **91**, 014515 (2015).

[104] F. Arute, K. Arya, R. Babbush, D. Bacon, J. C. Bardin, R. Barends, R. Biswas, S. Boixo, F. G. S. L. Brandao, D. A. Buell, B. Burkett, Y. Chen, Z. Chen, B. Chiaro, R. Collins, W. Courtney, A. Dunsworth, E. Farhi, B. Foxen, A. Fowler, C. Gidney, M. Giustina, R. Graff, K. Guerin, S. Habegger, M. P. Harrigan, M. J. Hartmann, A. Ho, M. Hoffmann, T. Huang, T. S. Humble, S. V. Isakov, E. Jeffrey, Z. Jiang, D. Kafri, K. Kechedzhi, J. Kelly, P. V. Klimov, S. Knysh, A. Korotkov, F. Kostritsa, D. Landhuis, M. Lindmark, E. Lucero, D. Lyakh, S. Mandra, J. R. McClean, M. McEwen, A. Megrant, X. Mi, K. Michielsen, M. Mohseni, J. Mutus, O. Naaman, M. Neeley, C. Neill, M. Y. Niu, E. Ostby, A. Petukhov, J. C. Platt, C. Quintana, E. G. Rieffel, P. Roushan, N. C. Rubin, D. Sank, K. J. Satzinger, V. Smelyanskiy, K. J. Sung, M. D. Trevithick, A. Vainsencher, B. Villalonga, T. White, Z. J. Yao, P. Yeh, A. Zalcman, H. Neven, and J. M. Martinis, Quantum supremacy using a programmable superconducting processor, Nature **574**, 505 (2019).

[105] W. Cai, J. Han, F. Mei, Y. Xu, Y. Ma, X. Li, H. Wang, Y. P. Song, Z.-Y. Xue, Z.-q. Yin, S. Jia, and L. Sun, Observation of Topological Magnon Insulator States in a Superconducting Circuit, Phys. Rev. Lett. **123**, 080501 (2019).

[106] B. Pérez-González, M. Bello, Á. Gómez-León, and G. Platero, SSH model with long-range hoppings: topology, driving and disorder, arXiv preprint arXiv:1802.03973 (2018).

[107] L. Li, Z. Xu, and S. Chen, Topological phases of generalized Su-Schrieffer-Heeger models, Phys. Rev. B **89**, 085111 (2014).

[108] C. Li and A. E. Miroshnichenko, Extended ssh model: Non-local couplings and non-monotonous edge states, Physics **1**, 2 (2019).

[109] X.-W. Xu, Y.-Z. Li, Z.-F. Liu, and A.-X. Chen, General bounded corner states in the two-dimensional Su-Schrieffer-Heeger model with intracellular next-nearest-neighbor hopping, Phys. Rev. A **101**, 063839 (2020).

[110] M. Atala, M. Aidelsburger, J. T. Barreiro, D. Abanin, T. Kitagawa, E. Demler, and I. Bloch, Direct measurement of the Zak phase in topological Bloch bands, Nat. Phys. **9**, 795 (2013).

[111] L. Li, C. Yang, and S. Chen, Winding numbers of phase transition points for one-dimensional topological systems, Europhys. Lett. **112**, 10004 (2015).

[112] E. J. Meier, F. A. An, and B. Gadway, Observation of the topological soliton state in the Su–Schrieffer–Heeger model, Nat. Commun. **7**, 1 (2016).

[113] J. Sirker, M. Maiti, N. Konstantinidis, and N. Sedlmayr, Boundary fidelity and entanglement in the symmetry protected topological phase of the SSH model, J. Stat. Mech. Theory Exp. **2014**, P10032 (2014).

[114] D. Xie, W. Gou, T. Xiao, B. Gadway, and B. Yan, Topological characterizations of an extended Su–Schrieffer–Heeger model, Npj Quantum Inf. **5**, 55 (2019).

[115] Y. He and C.-C. Chien, Non-Hermitian generalizations of extended Su–Schrieffer–Heeger models, J. Phys. Condens. Matter **33**, 085501 (2020).

[116] W. Nie and Y.-X. Liu, Bandgap-assisted quantum control of topological edge states in a cavity, Phys. Rev. Research **2**, 012076(R) (2020).

[117] D. J. Thouless, Quantization of particle transport, Phys. Rev. B **27**, 6083 (1983).

[118] M. Lohse, C. Schweizer, O. Zilberberg, M. Aidelsburger, and I. Bloch, A Thouless quantum pump with ultracold bosonic atoms in an optical superlattice, Nat. Phys. **12**, 350 (2016).

[119] S. Nakajima, T. Tomita, S. Taie, T. Ichinose, H. Ozawa, L. Wang, M. Troyer, and Y. Takahashi, Topological Thouless pumping of ultracold fermions, Nat. Phys. **12**, 296 (2016).

[120] J. Tangpanitanon, V. M. Bastidas, S. Al-Assam, P. Roushan, D. Jaksch, and D. G. Angelakis, Topological pumping of photons in nonlinear resonator arrays, Phys. Rev. Lett. **117**, 213603 (2016).

[121] S. Greschner, S. Mondal, and T. Mishra, Topological charge pumping of bound bosonic pairs, Phys. Rev. A **101**, 053630 (2020).

[122] K. Tschernig, Á. Jimenez-Galán, D. N. Christodoulides, M. Ivanov, K. Busch, M. A. Bandres, and A. Perez-Leija, Topological protection versus degree of entanglement of two-photon light in photonic topological insulators, Nat. Commun. **12**, 1 (2021).

[123] T. Haug, L. Amico, L.-C. Kwek, W. J. Munro, and V. M. Bastidas, Topological pumping of quantum correlations, Phys. Rev. Res. **2**, 013135 (2020).

[124] Y.-X. Du, Z.-T. Liang, Y.-C. Li, X.-X. Yue, Q.-X. Lv, W. Huang, X. Chen, H. Yan, and S.-L. Zhu, Experimental realization of stimulated Raman shortcut-to-adiabatic passage with cold atoms, Nat. Commun. **7**, 1 (2016).

[125] T. P. Harty, D. T. C. Allcock, C. J. Ballance, L. Guidoni, H. A. Janacek, N. M. Linke, D. N. Stacey, and D. M. Lucas, High-fidelity preparation, gates, memory, and readout of a trapped-ion quantum bit, Phys. Rev. Lett. **113**, 220501 (2014).

[126] Y.-X. Shen, L.-S. Zeng, Z.-G. Geng, D.-G. Zhao, Y.-G. Peng, and X.-F. Zhu, Acoustic adiabatic propagation based on topological pumping in a coupled multicavity chain lattice, Phys. Rev. Appl. **14**, 014043 (2020).

[127] Z.-G. Chen, W. Tang, R.-Y. Zhang, Z. Chen, and G. Ma, Landau-Zener Transition in the Dynamic Transfer of Acoustic Topological States, Phys. Rev. Lett. **126**, 054301 (2021).

[128] J. Koch, T. M. Yu, J. Gambetta, A. A. Houck, D. I. Schuster, J. Majer, A. Blais, M. H. Devoret, S. M. Girvin, and R. J. Schoelkopf, Charge-insensitive qubit design derived from the Cooper pair box, Phys. Rev. A **76**, 042319 (2007).

[129] X. Li, Y. Ma, J. Han, T. Chen, Y. Xu, W. Cai, H. Wang, Y. P. Song, Z.-Y. Xue, Z.-Q. Yin, and L. Sun, Perfect Quantum State Transfer in a Superconducting Qubit Chain with Parametrically Tunable Couplings, Phys. Rev. Appl. **10**, 054009 (2018).